CHALMERS
UNIVERSITY OF TECHNOLOGY

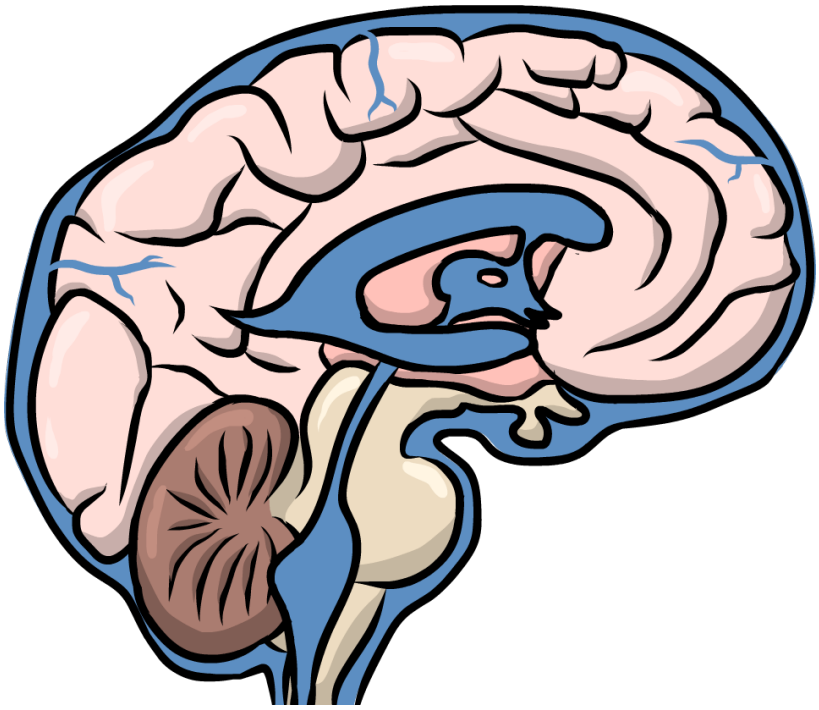

Powering intracranial pressure sensor implants via piezoelectric energy harvesting

A study on the possibilities of harvesting energy from the human brain using a lead-zirconate-titanate cantilever beam

Master's thesis in Biomedical engineering

Charlie Erndin Dahlberg

DEPARTMENT OF MICROTECHNOLOGY AND NANOSCIENCE

Chalmers University of Technology
Gothenburg, Sweden 2023
www.chalmers.se

Master's thesis 2023

Powering intracranial pressure sensor implants via piezoelectric energy harvesting

A study on the possibilities of harvesting energy from the human brain using a lead-zirconate-titanate cantilever beam

Charlie Erndin Dahlberg

CHALMERS
UNIVERSITY OF TECHNOLOGY

Department of Microtechnology and Nanoscience
Division of Electronics Material and Systems
Chalmers University of Technology

Powering intracranial pressure sensor implants via piezoelectric energy harvesting
A study on the possibilities of harvesting energy from the human brain using a lead-zirconate-titanate cantilever beam
Charlie Erndin Dahlberg

Supervisor: Per Lundgren, Department of Microtechnology and Nanoscience
Examiner: Maria Asplund, Department of Microtechnology and Nanoscience

Degree project 2023
Department of Microtechnology and Nanoscience
Division of Electronics Material and Systems
Chalmers University of Technology

Cover: The cerebral ventricular system of the human brain

Abstract

Intracranial pressure monitoring is conventionally done via an external ventricular drain or an implant probe where a wire protrudes through the skull. Such methods are cumbersome, costly, highly invasive and they constitute a significant risk of infection with each procedure. For long-term intracranial pressure monitoring, new types of implants which can be left inside of the patient are required in order to minimize the amount of surgery. Such implants can not be powered by batteries as batteries need to be replaced when they have been discharged. This thesis instead turns towards energy harvesting, and investigates whether energy can be harvested from the human brain by the means of a piezoelectric cantilever harvester, in order to power a pressure sensor implant. A literature review was conducted in order to examine the current state-of-the-art of energy harvesting inside the human body. A PZT (lead zirconate titanate) cantilever harvester was simulated together with a simple brain model in order to see how much power can be generated by placing the harvester on the brain surface. Results show that a simple 7x7 mm^2 thin plate bimorph PZT harvester can generate up to 2.6 nW. Additionally, a phantom brain test rig was constructed and pressurized in order to mimic the pressure dynamics inside the human brain. The system power requirements for a sensor implant with a transceiver would however amount to around 300 µW. Thus, a wake-up receiver system should be used where measurements are only taken sparsely for short durations. The power loss of supercapacitor leakage currents sets the lower limit of required harvesting output to roughly 1 µW. Meanwhile, the upper limit of what can be produced by a PZT brain harvester is 1.4 µW. Thus, powering a sensor implant by piezoelectric brain harvesting is theoretically possible, but the harvester must be very well optimized for the task.

Contents

Glossary

in vitro

Research done in a lab environment; not in a living organism. 28, 30

in vivo

Research done on or inside of a living organism. 11, 14, 26, 28–32, 58

bimorph

A cantilever consisting of two piezo-electric layers. 23, 24, 32, 33

edema

Swelling due to excessive accumulation of fluid between cells of connective tissue. 12

hemorrhage

Bleeding as a result of damaged blood vessels. 12, 13, 18

herniation

Shifting of the brain tissue from one space in the skull to another. 12, 13

hydrocephalus

Excessive accumulation of cerebrospinal fluid in the ventricles of the brain. 12, 13

poling

The process of exposing a piezoelectric sample to a strong electric field which aligns the sample's microscoping dipoles. 16, 18, 27

List of acronyms

AC alternating current 48, 50

AlN aluminium nitride 30

$BaTiO_3$ barium-titanate 21, 22

CPP cerebral perfusion pressure 13

CSF cerebrospinal fluid 12, 13, 18, 19, 39, 56, 57

DC direct current 48, 50

EVD external ventricular drain 10, 18, 19

FEM finite element method 31, 37, 44, 56, 57

FEP fluoroethylenepropylene 33–37

ICC intracranial compliance 39

ICP intra-cranial pressure 5, 10–13, 18–20, 31, 32, 37–40, 43, 47–49, 56, 58, 59

KNN potassium-sodium-niobate 29, 30

$LiNbO_3$ lithium-niobate 30

MAP mean arterial pressure 13

PEH piezoelectric energy harvester 20–24, 27–29, 31–33, 37, 49, 50, 54–58

PET polyethylene terephthalate 29

PLA polylactic acid 34

PMN lead-magnesium-niobate 29, 30, 58

PT lead-titanate 30

PVDF polyvinylidene-fluoride 21, 23, 26–30, 58

PZT lead-zirconate-titanate 3, 11, 15, 21–23, 26, 27, 29–32, 37, 41, 44–47, 52, 58, 59

RF radio frequency 14, 49

rGO reduced graphene oxide 23, 30

RMS root-mean-square 32, 46, 51

ZnO zinc-oxide 15, 16, 21–23, 27, 30, 58

Aknowledgements

I would like to thank Per Lundgren, my supervisor, for providing guidance and support and for always being available to help tackle various roadblocks along the way. I would also like to thank Maria Asplund, Lukas Matter and Shabir Afshar for their invaluable support throughout this thesis project.

1 Introduction

Monitoring the human body by measuring different biological signals is how we diagnose diseases or medical complications. Some of the most crucial bio-signals are found in or are connected to the bloodstream, such as heart rate or blood pressure. But while blood pressure is rather easy to measure using a sphygmomanometer [1], there are also pressure fluctuations inside your head, however these are not as easy to monitor. The brain is permeated by cerebrospinal fluid, which is separated from the cardiovascular system by the blood-brain barrier. One of the most common conventional methods for measuring intra-cranial pressure (ICP) today is external ventricular drain (EVD), where a hole is drilled and a catheter is inserted into the ventricles in the brain [2]. This method enables urgent treatment via fluid draining as well as measurement of the ICP. However, it is highly invasive and requires the catheter to be in place during the measurements, making it only suitable for short-term monitoring.

For less urgent scenarios and long-term ICP measurement however, a less cumbersome solution is needed. By instead implanting a wireless pressure sensor device inside the skull, the sensor could then be left inside the patient long-term, preferably for life. However, such a device would need to be powered without changing batteries or maintenance, since additional surgery brings increased risk of infection and economic cost for society. An alternative energy source is needed, one which exists inside the human body and is self-sustaining. In pursuit of such an energy source, this thesis looks at the brain itself. The human brain consumes roughly 20 W [3]. Would it therefore be possible to harvest energy from less useful brain actions, such as mechanical brain pulsations due to ICP fluctuations? The ability to harvest energy from the brain itself would enable medical implants to be self-sustaining and would open new doors for future implants.

This thesis aims towards investigating whether energy can be harvested directly from the human brain to power medical implants, with a focus on ICP sensors. The thesis begins with a brief introduction to ICP and what complications might arise from it, as well as an overview of energy harvesting and how it can be implemented in bio-medicine. Thereafter the physics and equations behind piezoelectricity is

described to introduce the reader to the field of piezoelectric harvesting specifically. In chapter 3, piezoelectric harvesting and different harvesting devices are described more thoroughly. Then, in chapter 4, the current state-of-the-art of *in vivo* energy harvesting is examined. Chapter 5 covers the methods used for the simulations and experiments conducted in this study. The simulations and experiments themselves are then presented in chapter 6. A thin plate cantilever lead-zirconate-titanate (PZT) harvester was simulated in Comsol and a phantom brain test rig was constructed. Additionally, chapter 6 also includes calculated estimations of available mechanical power in the brain as well as suggestions for how to implement an energy harvester inside a sensor implant system.

1.1 Aim and scope

The aim of this thesis is to investigate how much power a piezoelectric harvester can generate from the human brain in the context of powering an implanted ICP sensor. Human brain harvesting will then be compared with other state-of-the-art *in vivo* harvesting devices. Focus is therefore on the design of the harvester and how geometry, choice of material and different harvesting strategies can maximize the device's power output. Different harvester structures, such as cantilever, thin film and nanowire structures are discussed. However, simulations and practical experiments will only deal with cantilever harvesters. This is due to the fact that cantilever harvesters are geometrically less complex than e.g. nanowire structures. Although the fabrication process will not be discussed in detail, fundamental design choices such as choice of material and thickness of the piezoelectric and electrode layers will be investigated.

The harvester design is intended for harvesting mechanical energy from the human brain. The device is limited to a $1\,\mathrm{cm}^2$ footprint. A block diagram of the harvester as well as supporting components such as a storage unit, a rectifying component as well as a transceiver is produced. However, the study is primarily focused on the design of the harvester device itself. One aim of developing this harvester is to reduce the need of additional surgery after the device has been implanted. The harvester is therefore intended for long term, even lifetime use.

1.2 ICP physiology

The brain contains cerebrospinal fluid (CSF), a colorless liquid which transports nutrients from blood to neural cells and which is eventually reabsorbed into the cardiovascular system [4]. CSF flows through the brain ventricles, but it also flows outside of the brain and permeates the brain tissues through thin vessels (see Figure 1.1). The human brain has four different ventricles, but in this thesis "ventricles" will refer to the lateral ventricles, which are the largest ones. Under normal healthy conditions the CSF volume is kept fairly constant as excessive fluid is reabsorbed into the blood. Mean ICP can change throughout the day, as brain activity and respiratory activity etc. varies. Temporary elevation in ICP is normal, with mean ICP usually ranging between 7 - 15 mmHg for adults, relative to the atmospheric pressure [5]. However, if a patient experiences elevated ICP long term it might be life threatening [4].

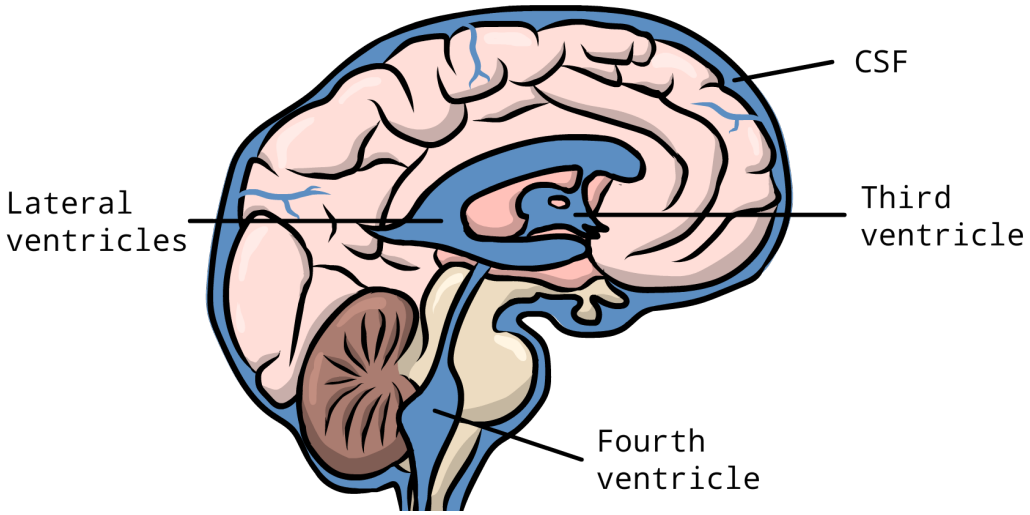

Figure 1.1: *The cerebral ventricular system of the human brain, where blue areas contain CSF. The brain has four ventricles: two lateral ventricles, the third ventricle and the fourth ventricle. The lateral ventricles are the largest fluid-filled cavity.*

Physical conditions that may lead to abruptly elevated ICP include traumatic brain injury, brain hemorrhage, brain herniation and hydrocephalus [5]. Brain trauma generally occurs as a result of an external force to the head, such as in the case of a fall or a collision. A brain hemorrhage, also called a cerebral hemorrhage, is a bleeding inside the brain. This may lead to edema (swelling) where the brain pushes against the skull which may result in herniation or damage to the brain stem [6].

Elevated ICP in the skull may lead to a pressure difference between cranial ICP and spinal ICP. This could lead to herniation, where the brain tissue is being pushed downwards. This could then damage vital structures such as the brainstem and could be life threatening. Abnormalities such as tumors, inflammation or head trauma can lead to hydrocephalus, which is a condition where excess CSF is accumulated inside the brain due to impaired draining, leading to increased ICP. Hydrocephalus is a serious condition which can be fatal if not treated [4].

Cerebral perfusion pressure (CPP) governs the blood flow and oxygen supply to the brain. The following relationship describes the connection between CPP and ICP:

$$CPP = MAP - ICP$$

where MAP is Mean Arterial Pressure. When the brain experiences elevated ICP, MAP increases as well to maintain a stable CPP. This may occur by increasing cardiac output or by altering arteriolar resistance. However, eventually the MAP is not be able to keep up, resulting in reduced CPP and potentially cerebral ischemia. For patients suffering from brain trauma or hemorrhage, quick ICP monitoring and treatment is crucial [5]. However for chronic diseases with an increased risk of hydrocephalus, long-term continuous monitoring of ICP is paramount.

1.3 Energy harvesting

Wireless electronic devices are conventionally powered by electrochemical batteries. In the field of implanted biomedical devices, changing batteries requires additional surgery, which increases the risk of infection for the patient as well as unwanted economic cost for the society [7]. Batteries also constitute a significant portion of the size and weight of small implants, which limits the device's scalability. Proposedly, the need for batteries can be bypassed by utilizing energy harvesting to power the device. There are multitudes of energy sources which are possible to harvest from, including chemical processes, electromagnetic radiation, thermal gradients and mechanical motion [8], [9]. Wind turbines or solar power plants are great

examples of large scale energy harvesting which is already well integrated in our society. Looking forward, piezoelectric pressure plates in road pavements have been suggested for harvesting mechanical energy from passing traffic [10], [11], while thermal harvesters have been suggested to capture and recycle wasteful heat energy in motors [12]. Biotechnology is a field which could benefit greatly from new energy harvesting methods, since medical devices implanted inside the body are hard to reach and therefore difficult to power with external power sources.

Various ways of *in vivo* harvesting have already been proposed, such as thin film devices harvesting mechanical power from the heart and aorta [13], [14], [15]. In fact, harvesting kinetic energy seems to be the most studied alternative for *in vivo* harvesting. There are no strong thermal gradients in the human body, since homeostasis keeps normal human body temperature between 36 and 38 °C [16]. Thus thermal harvesting would require parts of the device to be exposed to air in order to utilize the temperature gradient between room temperature and body temperature [17]. Alternatively, external stimuli in the form of a cooling device would be needed. Techniques such as radio frequency (RF) harvesting and ultrasound harvesting also need external activators, making energy harvesting more cumbersome and harder to perform continuously than a completely independent harvester. Chemical energy is plentiful in the human body, which is driven by metabolism, but it is hard to tap into chemical energy sources such as human mitochondria. Attempts have been made to develop bio-fuel cells which utilize redox reactions in the body as well as hydrovoltaic generators which aim to harvest electric energy from the interface between solid materials and liquids, mainly water. These are recently emerging harvesting technologies however, and they require more research as they suffer from low lifetimes and infection risks [7].

Compared to the previously mentioned power sources, mechanical power transfer is more abundant and easier to tap into. Various strategies have already been suggested for harvesting kinetic energy released from the human body; most are focused around harvesting mechanical energy from limb motion, muscle contractions, exhalation, heart beating or blood vessel pulsation [9], [18], [19], [14]. Many different mechanisms have been suggested or tried for electro-mechanical transduction in medical implants. Piezoelectric harvesters utilize the piezoelectric effect, where an

applied stress can directly affect the charge density of a polarised material [20]. Triboelectric harvesters can produce an electrical signal via free charge carriers which are transferred between two plates by friction. Electromagnetic harvesters utilize Faraday's law of induction, where a varying magnetic field, which can arise due to *e.g.* a permanent magnet being attached to a moving body part, induces an electric signal [17]. Electrostatic harvesters are capacitive devices which produce electric charge as the distance between two plates varies with body or organ movement. Because of the size limitations of a brain implant, piezoelectric harvesting seems to be the most promising strategy. Piezoelectric harvesters can be fabricated at micro-scale and also be integrated with micro-scale circuits [21]. Piezoelectric harvesting also benefits from high electro-mechanical coupling as well as high power density. Electro-mechanical coupling is a measurement of how efficient a harvester is in converting mechanical to electrical energy. This is a very important property and governs how much electrical power that can be generated for a given mechanical input signal. Power density is another crucial property which is a measurement of how much power can be generated for a given area or a given volume. When confined to a limited volume, power density becomes yet another governing property determining how much electrical power can be generated.

1.4 Piezoelectricity

A piezoelectric material has the ability to produce an electric response to a mechanical stimuli, or vice versa. The most common piezoelectric materials are ceramics with ionic bonds such as lead-zirconate-titanate (PZT) and zinc-oxide (ZnO) [7]. Their piezoelectric properties stem from their crystal lattices. Each unit cell consists of anions and cations, who share the same centre of charge when no mechanical strain is applied. However, when the material, and consequently individual unit cells, are strained, the negative and positive charge centres are separated. The unit cells thereby become microscopic dipoles, as shown in Figure 1.2 [22].

For other piezoelectric materials such as polymers or polymer-ceramic composites, the mechanism is similar except for the fact that molecular groups make up the microscopic dipoles rather than ions [8] [7]. However, for materials such as PZT,

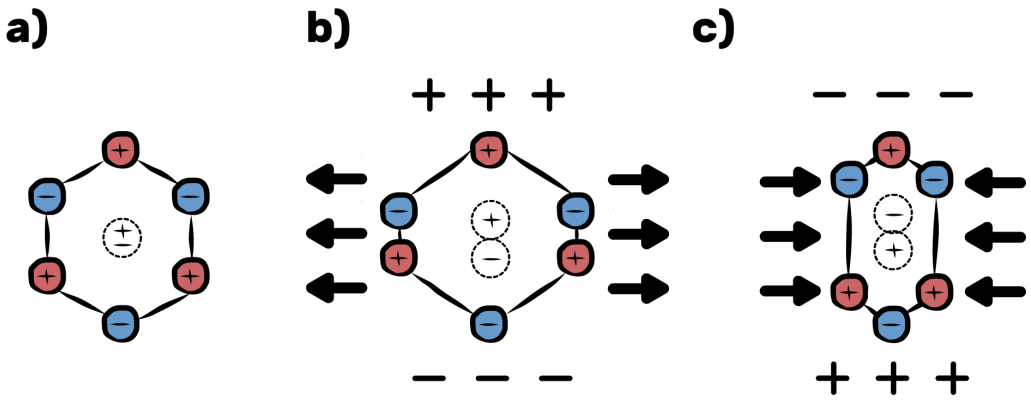

Figure 1.2: *The piezoelectric effect. A) Without external mechanical stimuli, the positive and negative charge centers overlap, resulting in a zero net charge. B) Mechanical stretching creates an asymmetry where the positive and negative charge centers are separated, and a potential difference is thus obtained across the unit cell, turning it into a dipole. C) Mechanical compression also induces a potential difference, but with reversed polarity.*

these microscopic dipoles are randomly oriented, leading to a net-zero dipole moment across the material. The dipoles need to be aligned, which is done via a process called poling. During poling, the material is exposed to a large electric field with a certain direction. Sometimes poling is performed in room temperature, but often higher temperatures are used [23]. The dipoles align themselves to the electric field and the direction of the field thus decides the poling direction. After the poling process, as the material is removed form the electric field, the dipoles remain aligned and the material then exhibits the ability to produce a net dipole moment when mechanically strained [24]. Thus, when an applied external force deforms a piezoelectric material, a dipole-moment and an electric potential difference is induced. Free charge carriers then move through the material to screen the induced potential, enabling the material to produce an electric current [7]. For other materials, such as ZnO, poling is not needed and the polar axis is instead determined by the crystal lattice orientation [21].

Piezoelectric materials are governed by the tensor equations [25]:

$$D = dT + \varepsilon E, \tag{1}$$

$$S = sT + dE. \tag{2}$$

Equation (1) describes how a piezoelectric material behaves when exposed to stress, which leads to an induced voltage. The electrical displacement D [C/m^2] depends on the piezoelectric coefficient d [C/N], the applied stress T [N/m^2], permittivity ε [F/m] and the electric field E [V/m]. In this configuration, d determines how much charge is generated for a given applied stress. Similarly, equation (2) shows the opposite behaviour, when an applied voltage is transduced to mechanical strain, which is dimensionless and is denoted as S. Then, d determines how much strain is induced for a given applied voltage. An optional, equivalent unit for the piezoelectric coefficient is [m/V], as:

$$\frac{C}{N} = \frac{C}{kg \cdot m \cdot s^{-2}} = \frac{C \cdot m}{kg \cdot m^2 \cdot s^{-2}} = \frac{m}{J/C} = m/V.$$

Finally, s [m^2/N] is the material's elastic compliance. Furthermore, the electrical displacement is related to induced voltage V according to:

$$D = \frac{\varepsilon V}{h}, \tag{3}$$

where h is the harvester thickness. When configured as an energy harvester, no external electric field is applied and thus by combining (1) and (3), the induced voltage can be described as a function of stress:

$$V = T\frac{dh}{\varepsilon}. \tag{4}$$

When discussing voltage output of piezoelectric materials, it is often more convenient to use the piezoelectric voltage coefficient g, defined as:

$$g = \frac{d}{\varepsilon}, \tag{5}$$

and equation (4) can then be expressed as simply:

$$V = Tgh. \tag{6}$$

Equations (1) and (2) are somewhat simplified, as the constants d and s are actually higher order tensors where each matrix element represents the respective constant

for a poling and strain direction. For a more accurate description, the piezoelectric constant d would be replaced by a matrix where for each element d_{ij}, i represents the strain direction and j represents the poling direction. Conventionally, the poling direction is considered to be along the third axis. This anisotropicity means that a piezoelectric harvester can be operated in two different modes [7]. In the d_{33} mode, voltage is induced along the same direction as the applied strain, while in the d_{31} mode, voltage is induced perpendicular to the applied strain.

2 Intracranial pressure monitoring

Intracranial pressure is generally measured directly and invasively, via inserted catheters and implants. This section outlines various monitoring procedures used today.

2.1 Current monitoring methods

External ventricular drain (EVD) is one of the most common methods used to monitor ICP today, where a catheter is inserted into one of the ventricles and directly measures pressure form the CSF (see Figure 2.1 5)) [5]. The main advantage of EVD is that it can be used for diagnostics as well as for treatment. It can monitor ICP with high accuracy but can also drain the ventricles in order to decrease pressure. However, EVD is a cumbersome and highly invasive procedure and therefore comes with a high risk of infection, especially for long-term monitoring. The risk of infection increases over time and reaches five percent after five days [5]. Moreover, catheter insertions may be difficult to perform, especially for patients with smaller ventricles or where swelling has occurred and insertions also risk causing hemorrhages. Another insert, which can be seen in Figure 2.1 6), that is used is the *subarachnoid* screw [5]. This screw is inserted by drilling through the skull and protrudes into the *subarachnoid* space, a fluid-filled region where CSF circulates outside of the brain [4]. This method is also both cumbersome and highly invasive and brings a high risk of infection, making it unsuitable for long-term monitoring.

Figure 2.1 7) shows various implants used to monitor ICP. These devices have

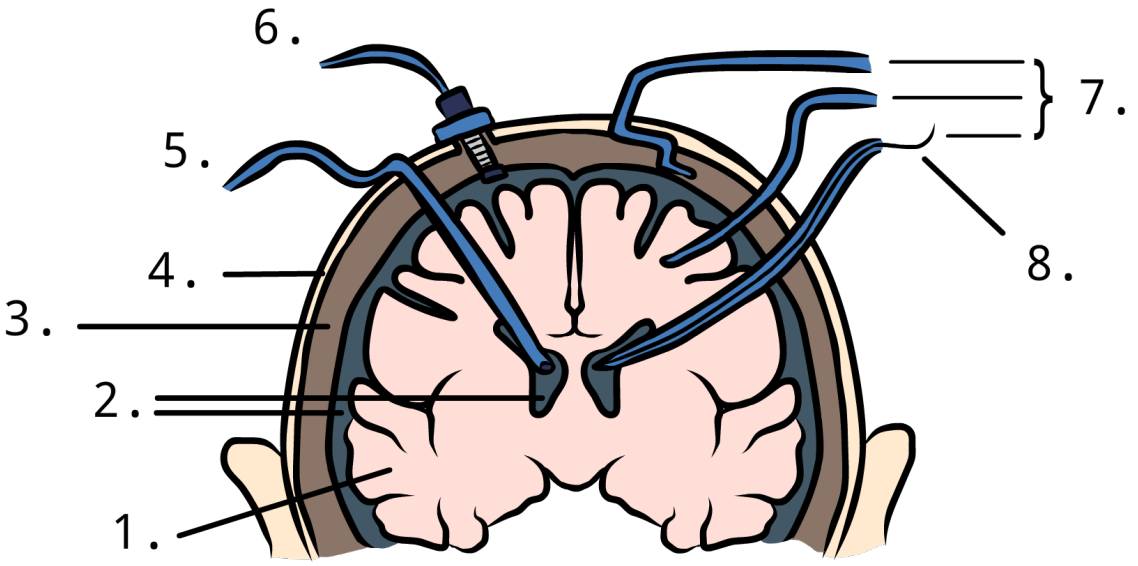

Figure 2.1: *Various ICP measuring methods: 1) Brain tissue (parenchyma). 2) The ventricles are located deep in the middle of the brain and contain CSF. CSF flows in various other parts of the brain, as well as in the subarachnoid space, just outside of the brain. 3) Arachnoid mater and Dura mater are membranes that contain blood vessels and cushion the brain. They are situated right beneath the skull bone (4). 5) EVD. 6) subarachnoid screw. 7) Implanted probes. 8) Optic fiber cable.*

a probe which can be inserted into different regions of the brain. The probe utilizes different transduction mechanisms for different sensors. The most widely used implants are strain gauge sensors, where pressure is measured using a flexible diaphragm, where the bending of the diaphragm is pressure-dependent [5]. In pneumatic sensors, a balloon is attached to the probe, which inflates and deflates with pressure variations. There are also fiber optic sensors where variations in pressure displace a mirror attached to the probe. The displacement in turn alters how much light is reflected into an optic cable, see Figure 2.1 8). These types of implantable probes are less cumbersome and more flexible than inserted sensors, as they can be placed in different brain regions. They also constitute a lower infection risk which makes them better candidates for long-term monitoring. It can be difficult to calibrate the sensors once implanted however, which is a major problem when a reliable, stable output over longer time spans is desirable [5].

2.2 Requirements for long-term monitoring

What all current ICP monitoring methods have in common is that they require a power source to operate. This is problematic as a wired power source is inconvenient

for the patient and batteries need to be replaced, requiring additional surgeries, each with a risk of causing an infection. Some studies actually indicate that because of the entailed risks of monitoring ICP today, it might in some cases do more harm than good and monitoring ICP may actually lead to increased mortality rates [26], [27]. Therefore, monitoring devices and procedures for long-term ICP monitoring must aim toward reducing the infection risk for each surgery, but also minimize the amount of surgery required. Finding alternative power sources such as by the means of energy harvesting is therefore of utmost importance.

2.3 Sensor power consumption

Conventional strain gauge sensors typically require an input of $3 - 5\,\mathrm{V}$ and approximately $5\,\mathrm{mA}$ [28]. A typical power consumption would then be $15 - 25\,\mathrm{mW}$. However, these commercial sensors are often optimized for sensitivity rather than power consumption. Numerous studies have shown that by optimizing biomedical pressure sensors through minimizing power consumption instead, power consumption could be reduced to approximately $100 - 300\,\mu\mathrm{W}$ [28], [29], [30].

3 Piezoelectric energy harvesters

Piezoelectric harvesting is one of the most promising harvesting techniques, as it can operate without any external power source, is resistant to environmental factors such as humidity, and enables high power densities, which is important for miniaturization [7]. A piezoelectric energy harvester (PEH) converts mechanical energy to electrical energy via a piezoelectric material, often attached to a protruding cantilever [8]. As the cantilever vibrates or is bent, the resulting stress is transferred to the piezoelectric layer, which then produces an electric dipole moment and an accumulated charge at the top and bottom of the layer. When the cantilever is connected to a circuit, a vibration or periodic bending input thus results in an alternating current output.

Mechanical energy harvesting can further be divided into vibrational harvesting and kinematic harvesting [21]. By attaching the harvesting device to a vibrational energy source, mechanical vibrations accelerate the PEH and the harvesting mechanism is

driven by the resonance response of the harvester. Vibrational harvesting is also often classified as inertial harvesting. This strategy is well adopted in literature and in applications as vibrations are a common ambient energy source. However, such a system is highly frequency dependent. Vibrational harvesters exhibit a high voltage output at its resonance frequency, but which is dampened as the operating frequency diverges from the resonance frequency [8]. This can be problematic as most forms of human movement are low frequency, on the order of single hertz, while the harvester's resonance frequency generally increases as it decreases in size. The resonance frequency can be lowered by *e.g.* using a spring-shaped design or by attaching a proof mass. However, such measures generally increases the weight or size of the harvester and thus it can be hard to reach resonance frequencies below the order of kilohertz for miniaturized systems, let alone single hertz [17]. If operating outside the resonance frequency, the PEH's power output may decrease significantly. Alternatively, kinematic harvesting is a more direct way to harvest mechanical energy, where the harvester movement or displacement is directly coupled to the source's mechanical movement. Such a system does not rely on resonance and is therefore less frequency-dependent. This makes kinematic harvesting well suited for the human brain as an energy source, whose pulsating frequency is in the order of single hertz.

3.1 Material and structure

The first implanted piezoelectric energy harvester (PEH) was introduced by Weng *et al.* in 2010 and utilized ZnO nanowires [31]. Piezoelectric materials can be divided into either crystals, such as quartz, ceramics such as ZnO, PZT and barium-titanate ($BaTiO_3$), or polymers such as polyvinylidene-fluoride (PVDF) [32] [24]. Piezoelectric crystals are single-crystalline materials which have a naturally asymmetric charge distribution, giving them piezoelectric properties. These materials are often used for high frequency applications due to their stability.

Piezoelectric ceramics are instead poly-crystalline and consist of small irregular grains with dipoles of random orientations. Poling is therefore required in order to align these microscopic dipoles. Ceramics exhibit the highest dielectric constants out of all piezoelectric materials, have a high electromechanical coupling factor and are

Table I: *Piezoelectric material properties. d = dielectric charge coefficient, ε_r = relative permittivity, s = elastic compliance, g = piezoelectric voltage coefficient, κ = electromechanical coupling factor.*

Parameter	PZT [33],[34],[35],[36],[37]	ZnO [33],[36]	$BaTiO_3$ [34]	PVDF [33],[34],[38]	Unit
d_{33}	60-593	6-9	190	24-33	pCN^{-1}
$\lvert d_{31}\rvert$	97-294	5	-	8	pCN^{-1}
ε_r	470-3400	10	1700	6-16	-
s	11-23	25-35	-	400-700	GPa^{-1}
g_{33}	0.019-0.036	0.1	0.013	0.17-0.43	VPa^{-1}
$\lvert g_{31}\rvert$	0.009-0.019	-	-	-	VPa^{-1}
κ_{33}	0.49-0.75	0.16-0.33	0.33-0.38	0.08-0.30	-
κ_{31}	0.22-0.39	-	-	0.12	-

therefore generally preferred over piezoelectric crystals in most applications. Most popular piezoelectric ceramics have a perovskite structure, meaning they follow the chemical formula of ABO_3, such as PZT ($Pb(Zr,Ti)O_3$) which is the most common PEH material due to its high piezoelectric coefficients d_{33} and d_{31} which can reach values roughly ten times as large as for *e.g.* polymer harvesters [20], [39]. Polymers have higher voltage coefficients, due to their low permittivity, but the coupling factor generally remains higher for PZT, as can be seen in Table I. Different variants of PZT exists such as PZT-4 or PZT-5H, sometimes called "hard" PZT and "soft" PZT respectively [21]. PZT-5H is slightly more elastic than PZT-4 and has one of the highest charge coefficients among PZT materials with $d_{33} = 593\,\mathrm{pC/N}$. Table I shows value intervals for various properties among common piezoelectric materials.

The *in vivo* applications of PZT are somewhat limited due to fragility, as it is brittle and has poor tensile strength, and the toxicity of lead is also problematic [22] [32]. ZnO is another common ceramic which has shown good biocompatibility but has a lower piezoelectric coefficient than PZT, which limits the harvester's output [20]. $BaTiO_3$ is a highly biocompatible material with higher piezoelectric coefficient than ZnO but lower than PZT [22] [20]. BZT-BCT has been introduced to replace PZT for *in vivo* applications with a piezoelectric coefficient as high as $620\,\mathrm{pCN^{-1}}$ [20]. Ceramics can also be infused with dopants to alter their properties [39].

Piezoelectric polymers can also exhibit piezoelectric properties [24]. Via poling, charged polymer chains attract and repel each other, increasing the polarizability. Among polymers, the most common material is PVDF. It is porous but flexible, easy to shape into thin films and has a low stiffness as well as low density [8], [22], [32], [24]. It is also highly biocompatible, and has a much higher piezoelectric voltage coefficient than ceramics [33]. However, it has a low piezoelectric constant making its electromechanical coupling factor only $\sim 10\%$ of PZT.

Some of the most promising recently developed PEH's have been composites of different piezoelectric materials. Polymer substrates can be infused with ceramic nanoparticles in order to achieve a compromise between the flexibility of polymers and the high dielectric coefficients of ceramics [40]. S. Azimi *et al.* showed that by combining PVDF with nanoparticles of ZnO and reduced graphene oxide (rGO), the dielectric coefficient could be significantly increased compared to regular PVDF PEH's [13]. Still, these composites also come with drawbacks such as reduced performance due to inhomogenity in the nanoparticle distribution and it is hard to polarize the nanoparticles efficiently as most of the polarization voltage is applied on the polymer due to its lower dielectric constant [40].

3.1.1 Cantilever beam

By far the most common piezoelectric harvester design is a protruding cantilever beam. Single-layer cantilevers consist of a piezoelectric layer attached to a support beam. Bimorph cantilevers have two piezoelectric layers, sometimes with a support layer sandwiched in between. The main purpose of the support layer is to increase mechanical strength. There is a trade-off between mechanical strength and reduced power output as a thicker support layer decreases the overall piezoelectric effect [41]. Similarly, stiffer support layers reduce output performance as well, so it is preferable to use an elastic material. Cantilever harvesters are commonly clamped at one end in order for the other end to perform a bending movement as a mechanical force is applied. If an external force is applied to the underside of a bimorph cantilever, an upwards bending motion will be induced (see Figure 3.1). Then, the lower piezoelectric layer will be stretched out perpendicular to the applied force and the upper layer will be compressed. Through the piezoelectric effect both layers will

then be polarized with opposite direction if they have the same poling direction or with the same direction if they have opposite poling directions (see Figure 3.2).

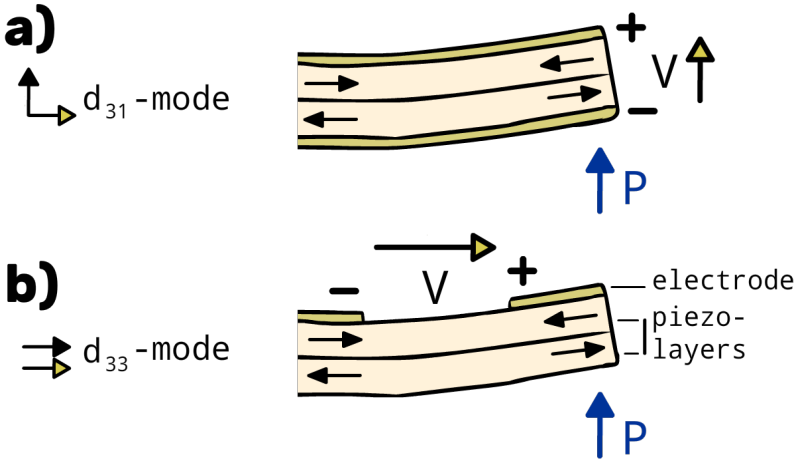

Figure 3.1: *When pressure acts on the cantilever (blue arrows), a bending motion occurs which induces a perpendicular mechanical strain in the cantilever. A PEH can operate either in a) d_{31} mode or in b) d_{33} mode. The first subscript indicates the direction of the induced mechanical strain (black arrows). The second subscript indicates along which direction the potential difference (V) is exploited (yellow arrows).*

Figure 3.1 shows how the harvester can operate in different modes, depending on how the electrodes are placed in relation to the induced stress. As can be seen in table I, the piezoelectrc coefficient and coupling factor is generally higher for d_{33} mode configurations compared to when operated in d_{31} mode. However, which mode yields the highest power output depends on the harvesting strategy. For cantilevers where the strain is induced perpendicularly to the bending motion, d_{31} mode is preferable [42]. For a bimorph cantilever design, the two piezoelectric layers can either be connected in series or in parallel, as shown in Figure 3.2. In a series configuration, the top and bottom electrode function as anode and cathode respectively, with the load connected between them. This requires that the two layers have opposite poling direction. In a parallel configuration, both the top and bottom electrode are connected to the same node, constituting either the anode or the cathode side, while the middle electrode functions as the other. Such a set up requires that both layers have the same poling direction. The voltage across the load is twice as large in a series configuration compared to the parallel one, but the current is halved. Thereby, the output power does not depend on the configuration.

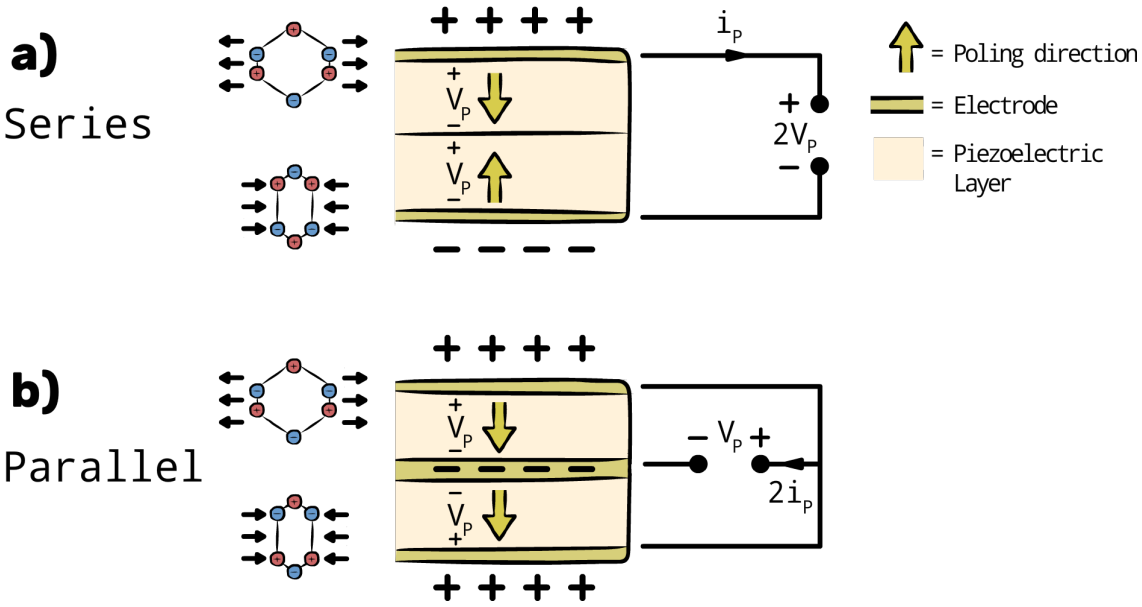

Figure 3.2: *How the harvester connects to the electrical circuit affects the voltage-current characteristics of the output signal. A) By connecting the two piezoelectric layers in series, the largest voltage output is obtained. This requires the two layers to have opposite poling direction as otherwise there would be negligible potential difference between the top and bottom plate. B) If the two piezoelectric layers are connected in parallel instead, the voltage is half that of the serial configuration while the current is doubled. For a parallel configuration, both layers need to have the same poling direction, and a middle electrode situated between the layers is needed.*

When it comes to the cantilever electrodes, covering the whole length of the beam with electrodes may not be optimal. The induced strain is generally strongest at the clamped end, and then decreases along the length of the beam, reaching its minimum at the free end. Consequently, the potential difference is also largest near the clamped end and lowest at the free end. Since the generated voltage will effectively be an average of the potential difference across the beam, there is an optimal electrode length. The free beam end produces a very low potential difference, and therefore only reduces the average potential. The optimal electrode length, as described by S. Du *et al.*, is one that stretches from the clamped end to where the induced strain has reached half the average strain across the covered length [43].

3.1.2 Thin films

Thin film harvesters are often used when the application demands a harvester with high flexibility, such as for harvesting energy *in vivo* from organs. Therefore, piezoelectric polymers such as PVDF are the most common materials used for thin films, as they exhibit high elasticity and are also considered to be more biocompatible than *e.g.* PZT [22]. The actual thickness of thin film harvesters can vary greatly, but are usually below 100 µm with some even reaching sub-micrometer thickness [44].

3.1.3 Nanoribbons

A major drawback of piezoelectric polymers such as PVDF is their low piecoelectric coefficients and electromechanical coupling constants, which limits their power output. One strategy to increase the power output is to place thin nanoribbons of a stiffer piezoelectric material with high electromechanical coupling such as PZT on a flexible polymer substrate. That way, a flexible harvester can be produced which increased coupling compared to purely polymeric thin films, but which retains much higher elasticity than purely ceramic harvesters [21].

3.1.4 Nanowire arrays

Another harvesting strategy is to place an array of densely packed nanowires, oriented either laterally or vertically, on top of some substrate. Ceramics such

as ZnO and BZT-BCT have been implemented in nanowire arrays, with the first demonstration taking place already in 2006 [22], [20]. More recently, PVDF and other polymers have also been used as nanowires [33]. One advantage of nanowires is that they can be used to achieve very low resonance frequencies, in the order of single hertz [7]. This means that they could potentially harvest vibrational energy from human organs such as the brain.

3.2 Harvesting performance

There is no clear convention in how piezoelectric harvesters are compared today. Output voltage, piezoelectric coefficient, electromechanical coupling factor as well as power density are some properties used to evaluate the performance of piezoelectric harvesters, but often only a few of these properties are stated for each PEH device, making comparisons between them difficult [45]. Furthermore, measuring the performance of a PEH by power density, *e.g.* by $\mu W/cm^3$, is not necessarily interesting for the reader as it directly depends on the input strain or stress of a specific experimental setup. Measuring power density in terms of volume is also not ideal in itself, as the height of piezoelectric nanowires or thin films *etc.* is often restricted to an order of micrometers. In this regard, an area power density is arguably a more useful metric.

The electromechanical coupling factor κ is a dimensionless measurement of the conversion efficiency between mechanical and electrical energy [46]:

$$\kappa^2 = \frac{d^2}{\varepsilon s} \tag{7}$$

Typical κ values for ceramic and crystal piezoelectrics are between 0.1 and 0.75 [46], [34]. As seen in table I, ceramic and specifically PZT harvesters possesses the highest coupling factors. Piezoelectric ceramics are also generally very stable over time and maintain their polarizability well. Over time however, depoling will occur to some extent reducing the polarizability of the material [25]. Formation of cracks and failure at the interface between piezoelectric material and electrode are some defects that can reduce piezoelectric performance. Additionally, the Curie temperature is a critical temperature at which a material loses its piezoelectric properties [32].

Because of these deficiencies, the power output of piezoelectric ceramics is reduced in a logarithmic manner as a function of time. From the study of S. R. Platt *et al.*, one can expect a $10 - 15\%$ loss in efficiency after 3 years and roughly 20% loss during a human lifetime and an operating frequency of 1 Hz [25].

4 Implanted harvesters

For the last ten years, various PEH devices have been suggested in research and have been implemented inside the bodies of animals such as pigs, bovine, dogs and rats [13], [47], [48], [49]. Some devices aim to harvest energy from limb motions, but when it comes to harvesting energy inside the body there is a strong focus on the heart and large arteries such as the aorta [15], [47], [50], [51]. These organs can be energy harvested because of the fact that they pulsate with a periodically shifting pressure, much like the brain [4]. This chapter will describe some of the current *in vivo* piezoelectric harvesting techniques.

4.1 State-of-the-art in vivo piezoelectric harvesting

Many researchers have steered toward using PVDF for harvesting implants because of its flexibility and proven biocompatibility [22]. In 2008, J. A. Potkay and K. Brooks investigated the possibilities of harvesting energy from the cardiovascular system by placing a harvester cuff around an artery [15]. In their *in vitro* study, they used a pressurized latex tube as a phantom artery. A cylindrical PVDF cuff harvester was clamped around the tubing and generated an average power of 6 nW. This idea was expanded upon in 2016 when X. Cheng *et al.* developed their own arterial cuff PVDF harvester [52]. The device was wrapped around the ascending aorta of a pig, yielding a maximum instantaneous output power of 40 nW. A generalized schematic of arterial cuff harvesters can be seen in Figure 4.1 B.

Around the same time, many researchers started looking into harvesting energy directly from the heart. In contrast to the arterial cuffs, researchers developing heart PEH's seem to favour ceramics rather than PVDF. This is likely due to the fact that a harvester attached to the heart surface experiences less curvature than a harvester wrapped around an artery. Less flexibility is then required and ceramics can instead

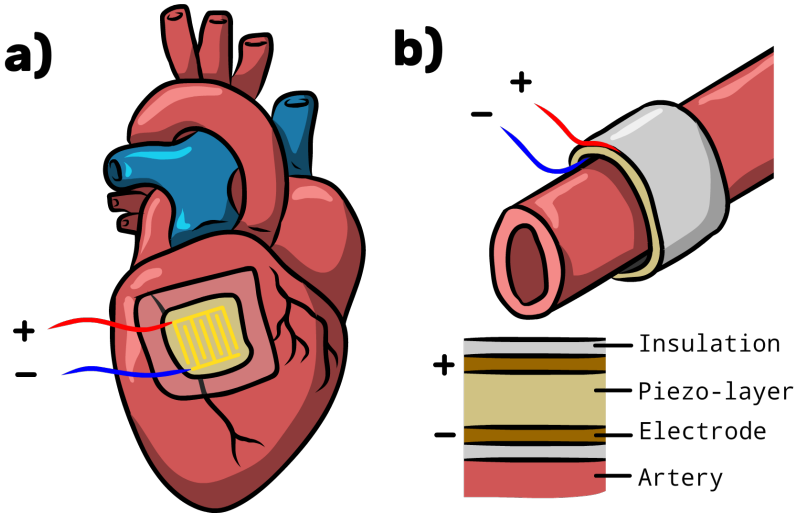

Figure 4.1: *Various PEH's have emerged to harvest energy from the cardiovascular system. A) Thin film PEH attached to the surface of a heart. The device is usually situated on top of a thin, flexible substrate made of e.g. PET. For the piezoelectric layer ceramics such as PZT is often used, which can utilize a zig-zag pattern or be placed as ribbons on a polymer film to achieve flexibility [47] [48]. B) Harvester cuff wrapped around an artery. The piezoelectric is sandwiched between two electrode layers. The device can be sheathed by a biocompatible material such as silicone [52].*

be used to exploit their higher piezoelectric charge coefficients. Regarding structure, thin films are used more or less exclusively for heart harvesting. Often the harvester device is situated on top of a thin substrate of polyethylene terephthalate (PET) (see Figure 4.1 A) [47], [48]. In some cases, the piezoelectric layer is shaped as a zig-zag structure on top of the substrate [47]. In other harvesters, PZT nanoribbons have been placed on top of a flexible polymer substrate [48], [50].

In 2014 G. T. Hwang *et al.* developed a thin film harvester aimed towards powering pace makers [49]. The material used for the piezoelectric layer was lead-magnesium-niobate (PMN)-PT, which exhibits a piezoelectric coefficient of 2500 pC, roughly four times higher than PZT. However, the harvester was powered by a linear motor so even with promising peak voltage and current output (4 V and 100 µA respectively), it is not clear how representative these values are for a harvester attached to an actual heart. Several heart harvesters have followed since, utilizing piezoelectric materials such as PZT, PVDF and potassium-sodium-niobate (KNN) [50], [13], [47]. Table II shows an overview of different *in vivo* harvesters along with their outputs. In many of these studies, as well as studies on aortic harvesting, average power output is not presented and is difficult to estimate. Often, only peak voltage and current

is presented, and the wave-forms are complex and often involve very high peaks. Therefore, instantaneous power is not necessarily a good indicator of performance, as it likely deviates significantly from the average power. In 2021 however, S. Azimi *et al.* implanted a thin film harvester on the heart of an adult dog [13]. They developed a composite of PVDF and ZnO in order to achieve a larger piezoelectric charge coefficient than for regular PVDF while still maintaining high flexibility. The harvester achieved a power density of $138\,\mu W/cm^3$, with 3.9 V peak voltage and 2.33 µA peak current.

Table II: *State-of-the-art in vivo piezoelectric harvesters.*

Energy source	Material	Structure	Peak voltage	Peak current	Power	Year	Ref.
Artery*	PVDF	Thin film	1.2 V	-	$24\,nW/cm^3$	2008	[15]
Motor*†	PMN-PT	Thin film	4 V	100 µA	-	2014	[49]
Bovine heart	PZT	nanoribbon	4 V	0.1 µA	-	2014	[48]
Pig aorta	PVDF	Thin film	1.5 V	0.3 µA	30 nW peak	2015	[51]
Pig heart	PZT	nanoribbon	1.5 V	-	-	2015	[50]
Pig aorta	PVDF	Thin film	1 V	-	40 nW peak	2016	[52]
Pig heart	$LiNbO_3$-doped KNN	Thin film	5 V	0.7 µA	-	2017	[47]
Pig heart	PMN-PZT	Thin film	17.8 V	1.75 µA	-	2017	[19]
Brain ventricles	AlN	Diaphragm	-	-	$12.6\,nW/cm^2$	2017	[53]
Pacemaker lead*‡	PVDF	Thin film	0.5 V	0.04 µA	-	2018	[54]
Pacemaker lead*‡	PVDF-ZnO	Thin film	3.22 V	-	-	2020	[55]
Dog Heart	PVDF-ZnO/rGO	Thin film	3.9 V	2.33 µA	$138\,\mu W/cm^3$	2021	[13]

**in vitro* testing, †0.36% strain at 0.3 Hz, ‡excited by a modal shaker at 1 Hz.

More recently, it has been suggested that harvesters could be wrapped around pacemaker leads [54], [55]. In 2020, Z. Xu *et al.* fabricated a thin film harvester from a PVDF-ZnO composite similar to the one used by S. Azimi *et al.* [55], [13]. The harvester is intended to be wrapped around a pacemaker lead, which is placed inside the right ventricle of the heart. A polymeric tube is used to sheath and

protect the harvester and a peak voltage of 3.22 V was obtained when exciting the harvester using a modal shaker. No *in vivo* experiments have yet been performed however.

Besides utilizing the cardiovascular system as an energy source, there are some other harvesting strategies that have been proposed. C. Dagdeviren *et al.* have designed a PZT nanoribbon PEH that can harvest energy from a bovine heart, but also from the lung and diaphragm movements [48]. They also utilized a structure where multiple thin films are stacked on top of each other and connected in parallel, in order to increase the voltage output. Some researchers have also looked at harvesting from the brain, such as L. Beker *et al.* who proposed a piezoelectric round diaphragm that harvests energy from ICP variations inside the brain ventricles [53]. Their device had a power density of 12.6 $\mathrm{nW/cm^2}$.

4.2 Cantilever structures versus thin films

Most research has been focused on harvesting energy using a thin film wrapped around a pulsating organ. One reason is that this strategy only requires the PEH to be attached to a single moving structure, in order to accelerate the piezoelectric element. A cantilever harvester, which instead harvests energy from a direct movement between two structures, needs to be attached to both of those structures. It has been argued that minimizing the required attachment points facilitates miniaturization [56]. However, single attachment point harvesters generally rely on vibrations and resonance dynamics rather than direct movements. Vibrational harvesters are known to suffer from poor frequency matching between high resonance frequency harvester devices and low frequency body motions and therefore vibration-invariant cantilever structures where the strain is bending-induced should not be ruled out [17].

Nano-structures such as nanowire and nanoribbon thin films are also generally more complex in their design and their small geometries make finite element method (FEM) simulations more computationally demanding than simulating a cantilever structure. Therefore, the harvester design suggested in this thesis instead utilizes a cantilever structure; partly to be able to perform FEM simulations, but also to

explore alternatives to thin film designs which have come to dominate the field of *in vivo* harvesting. While thin film harvesters require less points of attachments than cantilevers, a cantilever PEH benefits from less complex geometry which could make the fabrication process cheaper and easier.

5 Method

This chapter describes how the thesis was carried out; the simulations as well as the test rig experiments. First, the design process of the simulated harvester is outlined, where various settings, parameter values and design choices are presented. Then, the test rig set up is shown, with all the equipment used during experiments. Finally, the design process of the mold used to shape the phantom brain is described as well.

5.1 Comsol simulations

In order to estimate the voltage, current and electrical power output of a piezoelectric harvester placed on top of the brain surface, a model was built using Comsol. A simple square bimorph cantilever as well as a zig-zag shaped cantilever was modelled. The harvester geometry was built directly in Comsol where the pre-existing PZT-5H material was used for the piezoelectric layers and gold was used for the electrodes. When building the mesh, mesh size was set to the built-in option of 'fine'. Then, the simulated PEH's were evaluated using the built-in *frequency study* function, in order to generate a pulsating pressure stimuli:

$$p = Ae^{j\omega t}, \tag{8}$$

where t denotes time and $A = 3$ mmHg and $\omega = 0.94$ Hz were used, in order to obtain a varying pressure similar to the analyzed ICP waveform. The voltage and current peak amplitude outputs were recorded, as well as the mean power output by multiplying the voltage and current root-mean-square (RMS) values.

A square thin plate cantilever was simulated, with length and width $w = 7\,\text{mm}$, in order for it to fit inside a 1 cm diameter footprint. Optimal values for thickness of the

piezoelectric layers and load resistance were investigated by performing parametric sweeps. Preferably, the electrodes should be kept as thin as possible as to not affect the harvesters mechanical properties more than necessary. The electrode thickness was set to $d_{Au} = 100\,\text{nm}$, as decreasing the thickness further increased simulation time significantly while only affecting the results marginally. For the bimorph cantilever, the two piezoelectric layers were first connected in parallel and then in series in order to compare the output between the two configurations. For the serial connection, local coordinate systems were defined for the two piezoelectric layers, to achieve reverse poling direction between them. The zig-zag plate was obtained by cutting out five 200 µm wide segments of the thin plate, resulting in a 1 mm wide beam turning in a zig-zag pattern.

5.2 Construction of the phantom brain and experimental set up

A silicone phantom brain was molded and then pressurized in order to mimic the pressure dynamics in the brain. The purpose of the phantom brain was to see how much power could be generated by a PEH cantilever which is bent by the expansion and contraction of the phantom brain. This section describes experimental set up, the design of the molds as well as the molding process itself.

5.2.1 Pressure system

Figure 5.1 shows the experimental set up of the pressure system. In order to pressurize the phantom brain, a Fluigent FLPG+ pressure generator was used together with a VP18+ vacuum pump from LabTech in order to be able to also generate negative pressure. Both pressure sources were connected to a control unit where pressure could be adjusted by turning a knob or digitally from a connected computer. From the control unit, a 4 mm outer diameter tube was connected to a fluid reservoir containing colored water. The fluid reservoir's outlet was then connected to the phantom brain via a thinner 1/16" outer diameter fluoroethylenepropylene (FEP) tube. The FEP tube required an airtight connection to the silicone brain, but FEP is very similar to polytetrafluoreten (teflon) which is notoriously hard to bond. Permabond POP primer together with Permabond 2050

cyanoacrylate glue was used to bond two inserted FEP tubes with the silicone brain; one inlet and one outlet. The outlet tube was connected to a Fluigent pressure sensor and the sensor's outlet was connected to a beaker where the water was collected. When measuring the pressure output of the control unit or in the sensor, Fluigent's software OxyGEN was used to visualize all pressure signals and to plot various graphs.

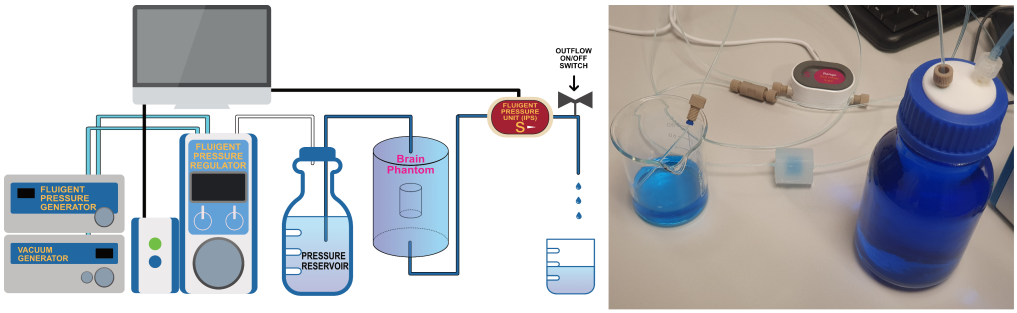

Figure 5.1: *Experimental set up for the pressure system. The left image shows a schematic illustration with all components used during the experiments. To the right is a photo taken of the final silicone brain phantom model. To the right of the phantom the fluid reservoir can be seen and to the left is the beaker collecting the water pumped through the phantom brain.*

5.2.2 Design of brain mold

A cylindrical phantom brain was cast with SF00 - RTV2 Silicone from Silikonfabrik, which has similar mechanical properties to the human brain. In the center of the phantom brain was a cavity representing the brain ventricles. Three casting mold prototypes were designed and tested: Mold A, B and C, as shown in Figure 5.2. Each casting mold was designed in Autodesk Inventor and then 3D-printed with a Prusa i3 MK3S printer using polylactic acid (PLA) filament. Mold A consisted of a mold frame with a half-cylinder shaped cavity where the silicone was poured. A cross-shaped support structure was placed on top of the mold, where a half-sphere shape protruded into the mold, in order to leave a half-sphere shaped cavity inside the silicone brain to represent one half of the ventricles. The mold yielded one half of the silicone brain. Casting the model in two halves enabled the protruding ventricle to be lifted out with the support cross after the silicone had solidified. If the whole model would have been cast in one step, the ventricle structure would not have been removable and would have been stuck inside the brain phantom. Twice, the liquid silicone was poured into the casting mold and treated for 15 minutes

in 50 °C, in order to yield two brain phantom halves. Then, the FEP inlet and outlet tubes were bonded with one of the brain-halves using the POP primer and the cyanoacrylate glue. Finally, both halves were bonded together using the same primer and glue.

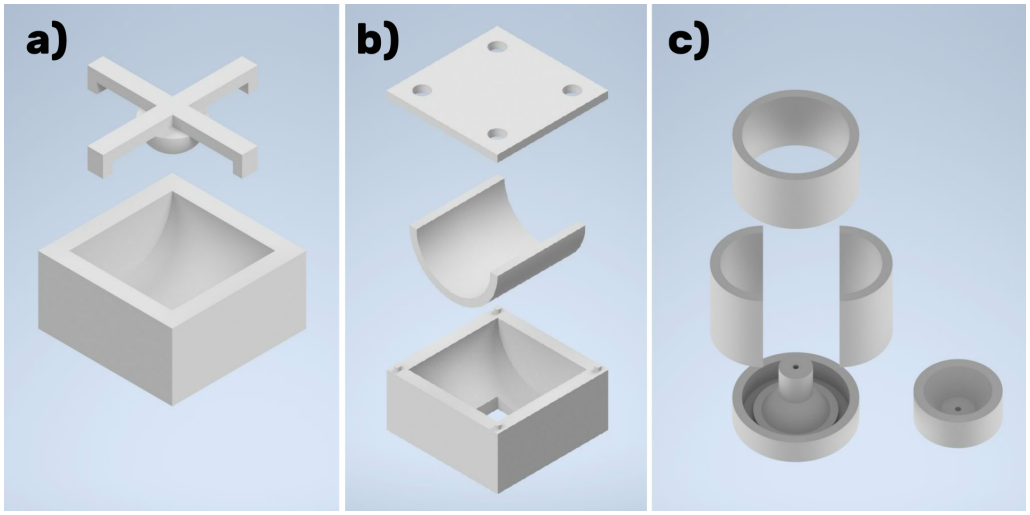

Figure 5.2: *Three mold designs were tested. a) Mold A consisted of a main frame and a cross-shaped support structure in order to shape the ventricle. b) Mold B converted the cross-shape to a flat lid and added a thin U-shaped plate to make it easier to remove the solidified silicone. c) Mold C utilized a different strategy where the whole silicone cylinder was cast in one procedure, except for the top which was cast separately, shaped as a conical frustum.*

Mold B (Figure 5.2 b) also consisted of a mold frame with a half-cylinder shaped cavity, but various adjustments were made to the design. Instead of casting the silicone directly in the mold frame, a thin U-shaped plate was placed inside the frame. The frame bottom had a hole, through which the U-shaped plate could be pushed out after the silicone had solidified, in order to reduce the risk of breaking the phantom when removing it from the mold. A flat lid with a protruding half-cylinder shape was used instead of the cross, in order to prevent artefacts from forming due to the cross shape. The ventricle design was changed from spherical to cylindrical so that the distance between the ventricle and the brain top/bottom surface would be more consistent. Four holes in the lid allowed excessive silicone to exit the mold. Instead of removing the halves immediately after solidifying, the halves were kept in their respective molds. Then, more silicone was mixed and applied to one of the halves as a thin layer, before joining the two molds together so that the halves contacted each other with the additional silicone in between used as glue instead

of the cyanoacrylate glue. The molds were then treated for a second time, in order for the newly applied silicone to bond the halves together. Instead of bonding the tubes to the silicone cylinder before joining the brain halves, the tubes were instead bonded afterwards by piercing the cylinder using a thin needle, and then inserting and gluing the tubes.

For mold C, the idea of bonding two halves together was abandoned and a different method for assembling the phantom brain was tested. The silicone cylinder cast by mold C still consisted of two parts, in order to be able to shape the ventricle. But rather than casting two halves, a main body was cast which was shaped as a solid cylinder with a cylindrical cavity and a open top, as shown in Figure 5.3. The second part was a shaped as a conical frustum and functioned as a lid to be placed on top of the main body.

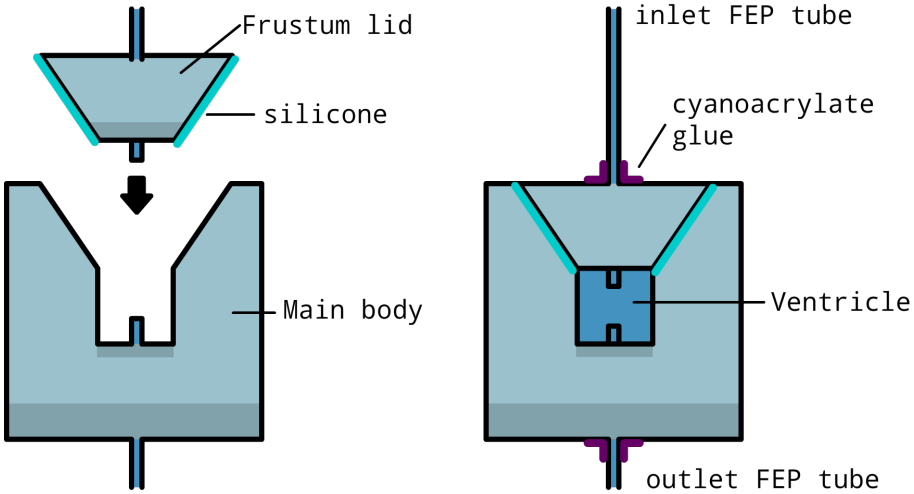

Figure 5.3: *Assembly of the final phantom brain. The frustum lid was bonded with the main body using the same silicone mix used for casting the main body and frustum lid, but as a glue. The cyanoacrylate glue was only used to bond the FEP tubes with the phantom.*

Mold C (Figure 5.2 c) consisted of two U-shaped plates which were joined to form a hollow cylinder. They were inserted into the bottom piece which had a protrusion shaped as the frustum lid. and the cylindrical ventricle. A tall ring piece was then used to keep the U-shaped plates in place. For the frustum lid, the separate single-piece mold seen to the right of Figure 5.2 c) was used. In contrast to mold A and B, mold C made it possible to mold the entire silicone main body in one procedure, rather than gluing together two halves. A 2 mm hole was also placed

through the center of the bottom piece as well as the frustum lid. The FEP inlet and outlet tubes were inserted into these holes before pouring the silicone so that as the silicone solidified, it would be molded around the tubes, which would then already be in the right position.

6 Results

In this chapter, the results are presented. First, the dynamics of ICP are investigated. After that, the mechanical power exerted by the human brain is calculated, in order to estimate the upper limit of how much power can be harvested from the brain. Then, the experimental results regarding the test rig are shown. Following that, FEM simulations of a PZT harvester and power, voltage and current outputs are presented. These results are then compared and a system design is drawn up as a suggestion for how to implement a PEH and an ICP sensor in a system.

6.1 Intracranial pressure waveform

In order to get a better understanding of the ICP waveform, a six hour ICP recording supplied by D. Farahmand was examined [57]. Fifteen seconds of the recording are shown in Figure 6.1 a). The whole data set was fourier-transformed in Matlab, which can be seen in Figure 6.1 c). There is a clear peak in the fourier domain at around 0.94 Hz which seems to correspond with the triple-peak structures in Figure 6.1 a). There is also a peak at 0.24 Hz which most likely corresponds with the slower periodicity in Figure 6.1 a), of which three periods can be seen. The cause of the 0.24 Hz frequency is not known, but patient breathing seems likely, as normal respiratory rate lies between $0.20-0.33$ Hz [58]. The 0.94 Hz frequency is compatible with a normal patient heart rate [4].

However, mean ICP as well as the amplitude can vary significantly even during normal activities. Figure 6.1 b) shows another extract from the ICP data supplied by D. Farahmand. This extract is from a later part of the recording, where the patient experienced a fifteen minute long period of increased ICP compared to the period shown in Figure 6.1 a). The ICP wave of this elevated period has a peak-to-peak pressure of around 10 mmHg, compared to the peak-to-peak pressure

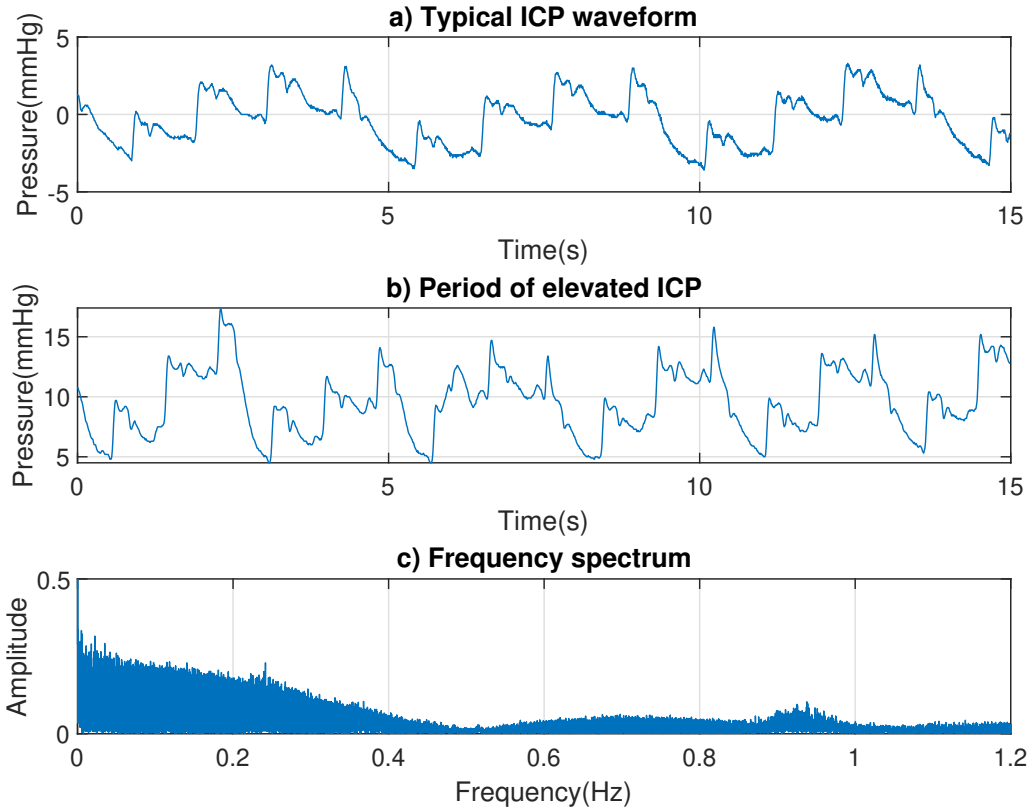

Figure 6.1: *ICP recordings plotted in Matlab. a) ICP waveform including a roughly 12 periods of a fast wave with three distinct peaks, as well as a slower wave where three periods can be seen. b) Different part of the ICP recording, where the pressure was significantly elevated. c) Spectral analysis of the entire 6 hour recording, showing two peaks at 0.94 Hz and 0.24 Hz respectively.*

of around 6 mmHg in Figure 6.1 a). The cause and nature of such periods with elevated ICP are hard to determine, however they appear similar to "B waves", which are temporary elevations of ICP where the mean pressure can increase by up to 20 mmHg. The concept of B waves has been around since the 1960's and they may appear in healthy patients although seem to be more common in patients with neurological dysfunctions [59].

6.2 Available power in the human brain

Most research has been focused on harvesting energy from the heart or from arteries, with little attention given to the brain. However, strategies developed to harvest energy from the cardiovascular system could be applicable to brain harvesting as well. The brain is a pulsating organ which experiences fluctuations in ICP, similar to how the heart or the aorta pulsate. Furthermore, decently sized arteries such as the right external and internal carotid are situated close to the brain and energy harvested from them could potentially be used to power brain implants. However, The pulsating pressure of cranial arteries and the CSF are significantly lower than that of the heart or aorta, which constitutes a major challenge. The heart has a pulse pressure of 40 mmHg, while the ICP pulse pressure of the brain is roughly $4 - 8$ mmHg, as seen in Figure 6.1.

The work W_{Brain} performed by the brain depends on the ICP pressure variation Δp, as well as the pressure-induced volume change ΔV:

$$W_{Brain} = \Delta p \cdot \Delta V. \tag{9}$$

The volume change can be described as a non-linear function of Δp, where the volume expansion becomes more pressure-sensitive with increasing pressure. However, for a rough estimation, the relationship can be approximated to be linear:

$$\Delta V = ICC_{Avg} \cdot \Delta p, \tag{10}$$

where intracranial compliance (ICC) is a measurement of how much the brain swells for a given amount of pressure. $ICC_{Avg} \approx 0.68$ mL/mmHg is an average value calculated by G. Portella *et al.* [60].

Then, by multiplying the work performed with the patient heart rate f_{heart}, the available power is obtained:

$$P_{Tot} = W_{Brain} \cdot f_{heart}. \tag{11}$$

The resting heart rate for adults range between $40 - 120$ BPM, corresponding to $0.7 - 2$ Hz [4]. Further, the available power on a $1\,\mathrm{cm}^2$ footprint can then be obtained:

$$P_{1cm^2} = P_{Tot}\frac{1}{A_{Brain}} \cdot \chi, \tag{12}$$

where $A_{Brain} \approx 1692\,\mathrm{cm}^2$ is the average brain surface area, which was calculated by H. Lemaitre *et al.* [61]. $\chi \approx 1/3$ is a compensation factor since about two thirds of the total cortical surface area is located inside folds and is therefore unavailable for energy harvesting [62]. Combining (9) - (12) and using the parameter values in Table III, the available mechanical power for harvesting on a $1\,\mathrm{cm}^2$ footprint is likely in the order of micro-Watts.

Table III: *Parameter values used during calculations.*

Parameter	Value	Unit
Δp	$4 - 8$	mmHg
ICC_{Avg}	0.68 ± 0.3 [60]	mL/mmHg
f_{heart}	$0.7 - 2$ [4]	Hz
A_{Brain}	1692 ± 172 [61]	cm^2
χ	1/3 [62]	-
P_{Tot}	$0.6 - 17$	mW
P_{1cm^2}	$0.1 - 3.7$	µW

Equations (9) - (11) indicate that energy harvested from the brain has a quadratic dependency on the pulsation pressure,

$$P = ICC_{Avg} \cdot \Delta p^2,$$

meaning that the power output of a brain harvester would be significantly lower than that of a heart harvester. However, unlike a pacemaker, a brain implant such as a ICP sensor does not necessarily have to be switched on at all times. By measuring ICP only a couple of times each day, rather than continuously at all times, the power requirements could be significantly reduced. Combining the estimated mechanical

power exerted from a $1\,\mathrm{cm}^2$ footprint of the brain surface $P_{1cm^2} = 0.1 - 3.7\,\mu\mathrm{W}$, with typical PZT coupling factor values $\kappa_{31} = 0.22 - 0.39$, the theoretical limit of piezoelectric brain harvesting using a PZT bending cantilever structure appear to lie in the range of $0.02 - 1.4\,\mu\mathrm{W}$.

6.3 Phantom brain test rig

The three mold designs mentioned in chapter 5: A, B and C, were all tested. The final prototype, mold C, is shown in Figure 6.2 a) and b), together with the cast silicone phantom brain. Mold A and B were each designed to only produce half the phantom brain, and thus for both molds, two halves were cast and glued together. However, the glue introduced several issues. As can be seen in Figure 6.2 c), once the glue had dried it produced a "scarring" effect on the silicone brain. The dried glue was much more brittle than the silicone and when the phantom brain was pressurized, cracks formed in the dried glue and the phantom brain started leaking. In several instances, the glue also ended up on the inserted tubes while gluing the halves together, resulting in the glue drying the tube ends and obstructing the flow. The glue had rather low viscosity, and thus any excessive glue that was applied spread to cover parts of the silicone surface, especially the top and the bottom. When the glue spread out across the phantom surface, an unwanted scarring effect occurred, which risked altering the mechanical properties of the phantom brain.

Instead of having to glue two halves together, mold C was able to cast most of the phantom brain in one instance. Only the frustum lid was cast separately and as the two silicone pieces were bonded together using silicone, only small amounts of glue were required to fasten the tubes. Thus, a much smoother and resilient phantom brain was produced, as seen in Figure 6.2 d).

The phantom brain was connected to the pressure system but when a sinusoidal pressure input with an amplitude of 3 mmHg and a frequency of 0.94 Hz was used, no mechanical response was observed from the phantom brain and no change in pressure was observed at the output side of the phantom. When testing different input signals, it was observed that the pressure measured after the phantom was

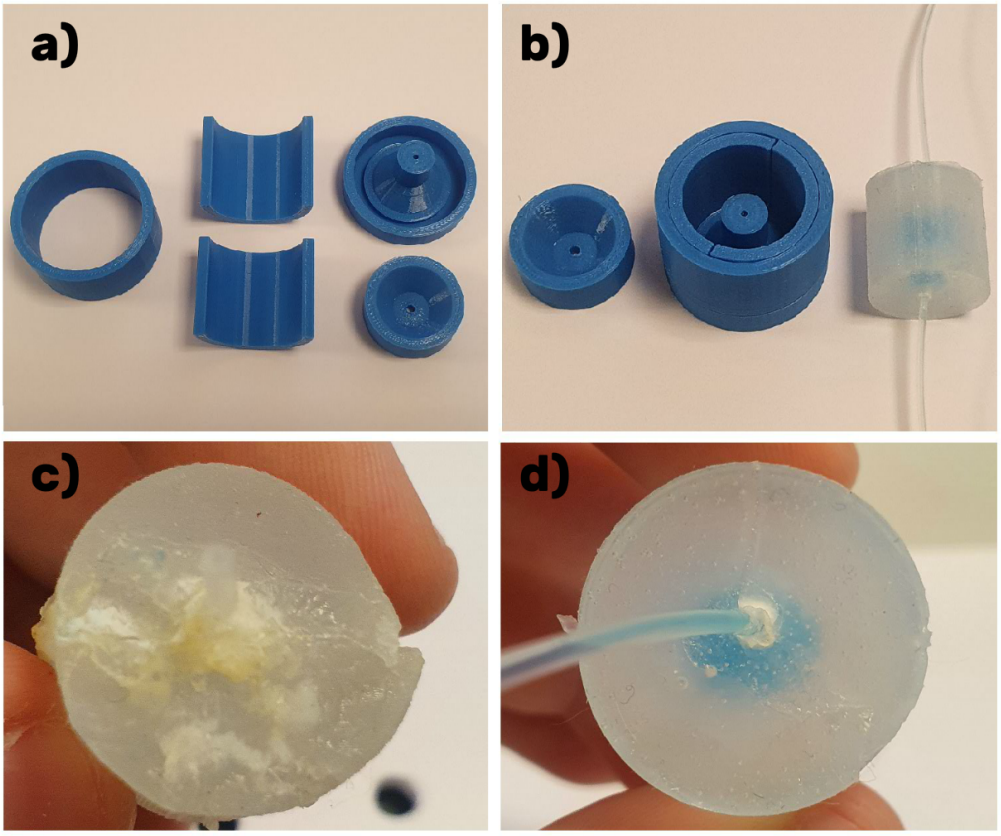

Figure 6.2: *Silicone phantom brain. a) 3D-printed mold C disassembled. b) Assembled mold C with separate smaller mold for the frustum lid. c) The initial attempts of gluing together two half-cylinders resulted scarring on the phantom surface. d) The phantom brain cast using mold C had a much smoother appearance as less cyanoacrylate glue was needed.*

significantly dampened. Additionally, there seemed to be an inertia in the system which made fast pressure variations impossible. A stronger and slower pressure signal was generated, with a 38 mmHg amplitude, frequency of 0.2 Hz and a 38 mmHg offset. Figure 6.3 a) shows that measured pressure after the phantom (green) was still both heavily dampened and slightly delayed compared to the generated pressure (red). Again, no mechanical response could be seen or felt from the phantom. Figure 6.3 b) shows a generated pressure with an 150 mmHg amplitude, frequency of 0.2 Hz and a 150 mmHg offset. However, the recorded pressure after the phantom hardly changed at all. Eventually, the silicone bonding between the frustum lid and the rest of the phantom gave way and the phantom started leaking, which can be seen by the measured pressure drop in 6.3 b).

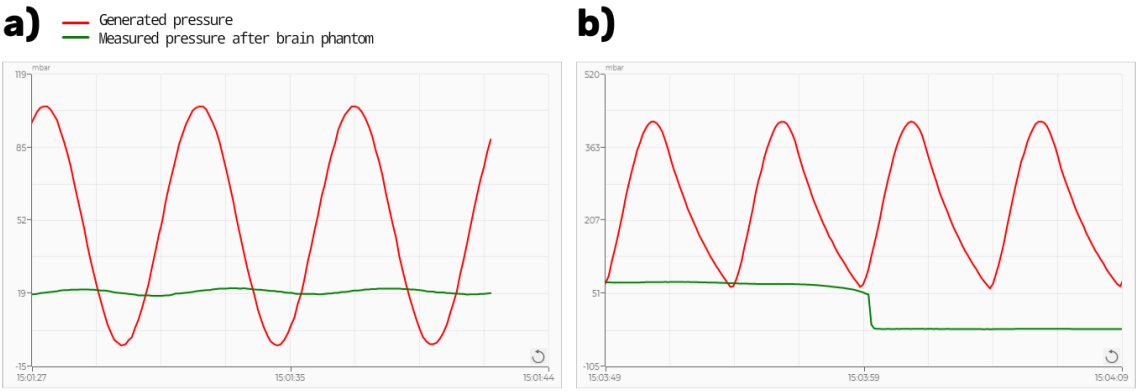

Figure 6.3: *Pressure measured before and after the brain phantom. a) The red graph shows the pressure output from the generator. The green graph shows the pressure measured by the pressure sensor connected to the brain phantom's outlet. b) When increasing the pressure, the bonding between the main body and frustum lid ruptured, as can be seen by the pressure drop in the pressure sensor.*

6.4 Simulated piezoelectric harvester

As seen in Figure 6.1, the ICP waveform is complex and is a superposition of at least two signals with different frequencies. This makes simulating the pressure dynamics inside the brain complicated. When performing a frequency study in Comsol, parameters can have a time dependency, but that dependency is limited in complexity to equation (8). This means that the simulated ICP signal is limited to a single frequency. Thus, during simulations the slower variations were ignored and equation (8) was used as the ICP signal, with $p = 3$ mmHg and $f = 0.94$ Hz.

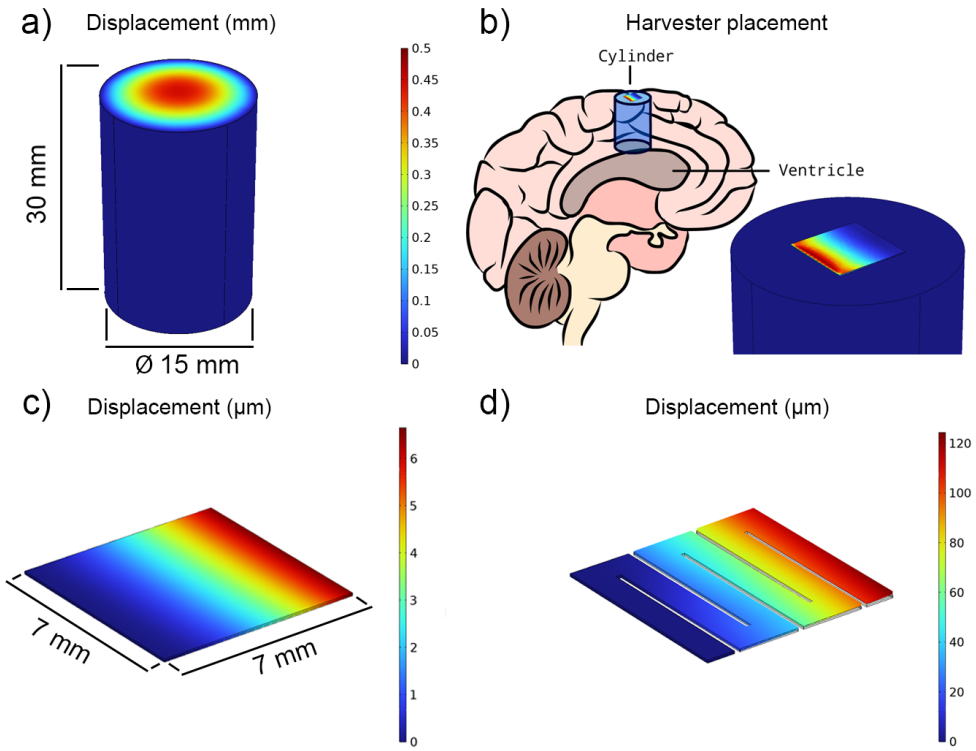

Figure 6.4: *FEM simulations of a PZT harvester in Comsol. a) A cylinder with mechanical properties similar to the human brain was pressurized from beneath. b) The cylinder is meant to mimic a cut-out of a human brain stretching from the ventricle to the brain surface. The harvester was placed directly on top of the cylinder during simulations. c) Thin plate harvester. The colormap shows displacement of the free end when the harvester is bent. d) Zig-zag plate harvester. The displacement is significantly increased compared to the thin plate harvester due to the zig-zag structure enabling higher flexibility.*

In Comsol, designing a complete brain was not feasible. A simplified cylindrical shape was therefore used to mimic mechanical properties of the human brain. The cylinder was 30 mm high and 15 mm in diameter, as it was meant to represent a cut-out of a human brain stretching from the ventricles to the brain cortex, as seen in Figure 6.4 b). The mechanical properties of the brain cylinder was chosen as to mimic the properties of a human brain, with a Young's modulus of $E = 1.5\,\text{kPa}$, Poisson ratio $v = 0.45$ and a density of $\rho = 1046\,\text{kg/m}^3$. Two harvesters were simulated; a 7 x 7mm^2 thin plate (Figure 6.4 c), as well as another plate with the same dimensions but with a zig-zag pattern (Figure 6.4 d), in order to increase flexibility.

The harvester consisted of five layers: two piezoelectric layers as well as three thin electrodes. PZT-5H was used for the piezoelectric layers and gold was used for the electrodes. In order for the electrodes not to affect the harvester's mechanical properties more than necessary they were made as thin as possible without making computations excessively slow. Of the three 50 nm thick electrodes, one was placed at the bottom of the harvester, one at the top, and one sandwiched between the two piezoelectric layers. This is the same parallel configuration as was shown in Figure 3.2. A load resistor was connected between the edge electrodes and the middle electrode with an initial resistance of 6 MΩ. During all simulations a pressure was applied uniformly to the underside of the brain cylinder. For both the thin plate and the zig-zag thin plate harvester designs, the harvester was placed on top of the cylinder brain, and one end of the harvester was then fixated, preventing it from move during the simulations. The lateral surface of the brain cylinder was also fixated, so that when pressurized from the beneath the cylinder was locked in place, but the top surface was still able to bulge outwards. When applying pressure from beneath, the induced stress then propagated through the brain cylinder and towards the harvester, thereby inducing a bending motion in the harvester.

As can be seen in Figure 6.4 a), The center of the cylinder brain's top surface expands 0.5 mm when the bottom surface of the cylinder is pressurized. Figure 6.4 c) and d) shows that when the harvester is placed on top of the brain cylinder, the displacement is significantly smaller; 6 µm for the thin plate design and 120 µm for the zig-zag design, indicating that the brain compresses as it pushes against the

harvester.

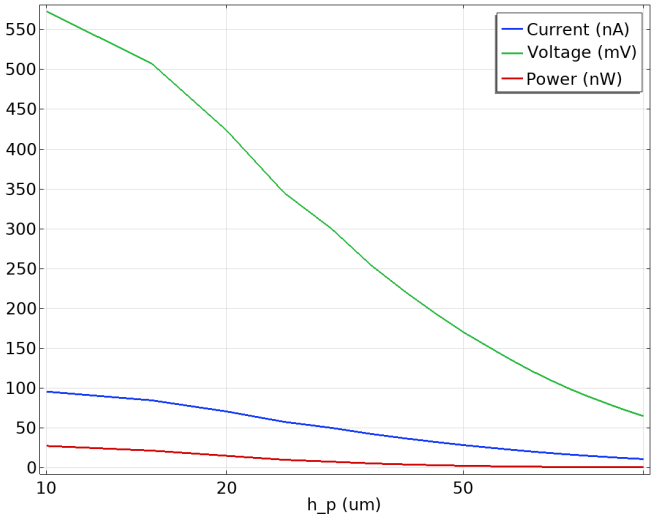

Figure 6.5: *Harvester output for different thickness h_p of each piezo-electric layer.* $6\,\mathrm{M\Omega}$ *were used for the load resistance.*

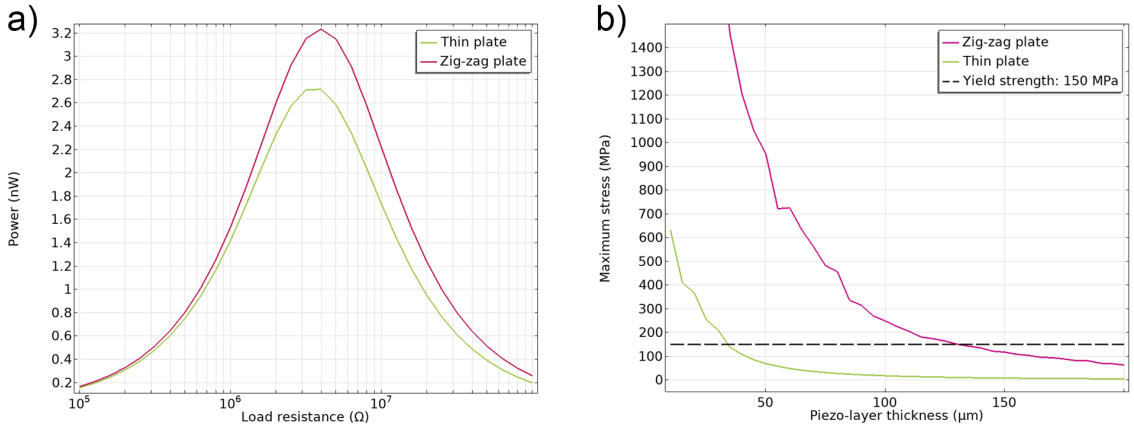

Figure 6.6: *Comparisons between the thin plate and the zig-zag plate design. a) Average power output for different load resistances. b) The highest stress recorded throughout the harvester for different thickness of the piezoelectric layers.*

A parametric sweep was then conducted to find the optimal thickness of the PZT layers. Figure 6.5 shows how the voltage, current and power output increases as the thickness decreases. The output voltage is the RMS voltage measured across the load resistor and the output current is measured as the RMS current going through the load resistor when the cylinder is pressurized from beneath. Thinner structures are more fragile and therefore another parametric sweep was conducted in order to see how much pressure the harvester could experience before it fractured. PZT-5H has a yield strength of 150 MPa, which means that if the stress inside the

harvester reaches similar levels, the harvester may break [63]. While normal ICP is around $7 - 15$ mmHg, periods of elevated ICP do occur and in extreme cases ICP levels as high as 90 mmHg have been recorded [64]. Figure 6.6 shows a comparison between the thin plate harvester and the zig-zag plate harvester regarding power output and stress resilience. Utilizing the zig-zag plate structure improves the power output slightly, from an average power of 2.7 nW to 3.2 nW, as seen in Figure 6.6 a). However, the zig-zag structure is much more fragile. Figure 6.6 b) shows the maximum stress measured inside the harvester when a constant pressure of 100 mmHg is applied to the underside of the brain cylinder. The thin plate harvester experiences stress equal to its yield strength when the PZT layer thickness decreases below 35 µm. The zig-zag plate harvester experiences similar stress levels already at 135 µm. Figure 6.7 shows the result of another parametric sweep. This time the output power was plotted for varying pressure amplitudes as well as for different frequencies, in order to investigate how variations in the ICP wave might affect the harvester performance. As can be seen, the power output increases for higher frequencies.

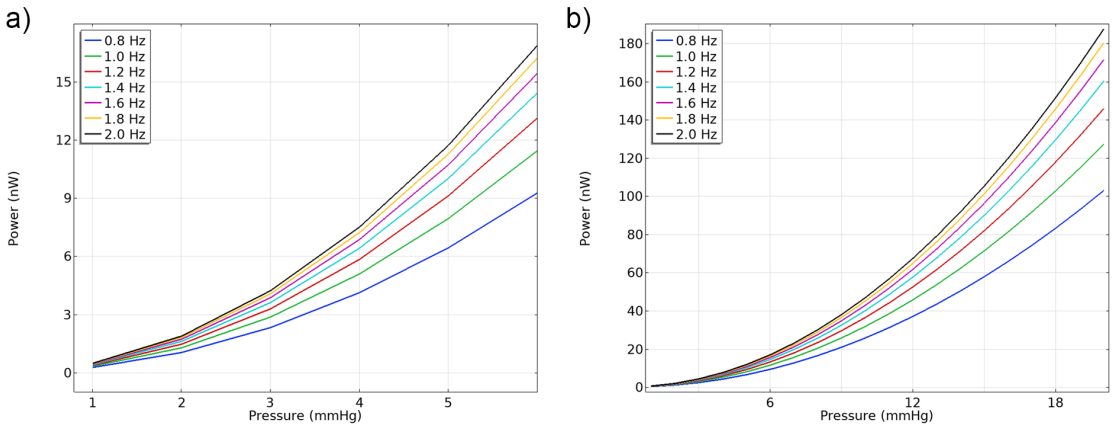

Figure 6.7: *Average power output for different amplitudes in the simulated ICP input. a) normal amplitude values. b) Same graph but including larger amplitude values to highlight the strong pressure-dependency of the power output.*

In order to verify that the power output was identical for both the parallel and serial configuration discussed in section 3.1.1, both confgurations were evaluated using the real part of $3e^{j0.94 \cdot 2\pi \cdot t}$mmHg as input pressure. Figure 6.8 a) shows that the peak pressure output is the same for both configurations, although the optimal load resistance has shifted. In Figure 6.8 b) the voltage and current output is

plotted for both configurations. The parallel configuration produces 140 mV peak voltage and 26 nA peak current at its optimal load resistance of 4 MΩ and the serial configuration produces 280 mV peak voltage and 13 nA peak current at its optimal load resistance of 15 MΩ.

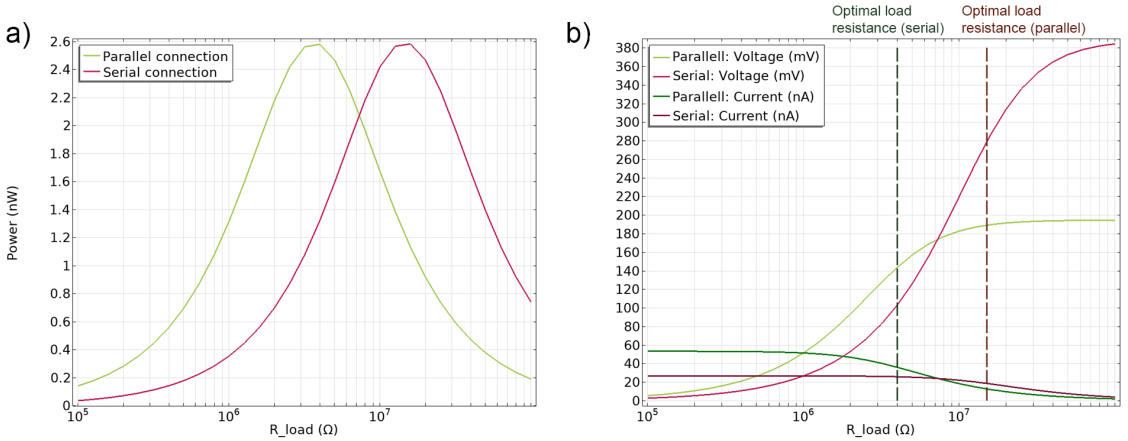

Figure 6.8: *Outputs for the piezo-electric layers connected in parallel as well as in series. a) Average power output. b) Peak voltage and peak current output.*

6.5 System design

The harvester must be able to generate enough power to supply the ICP sensor, and preferably additional components such as a transceiver as well. Previous work by A. Vyas indicates that the system's power requirement will likely range between µW and mW [8]. Figure 6.9 shows a block diagram of the system proposed in this thesis. After the harvester, a rectifier is needed to convert alternating current (AC) to direct current (DC). The generated voltage must be boosted in order to be large enough to overcome the rectifier diode's forward bias as well as to match the input voltage of the connected load. Additionally, a storage capacitor will be needed in order to store the harvested energy.

6.5.1 Power requirements

The purpose of a sensor is to extract data and thus an implanted ICP sensor would require a transmitter in order to send the collected data to an external device situated outside the body. A transceiver would be even more beneficial, as it consists of both a transmitter and a receiver. We can already see from the results in Figure

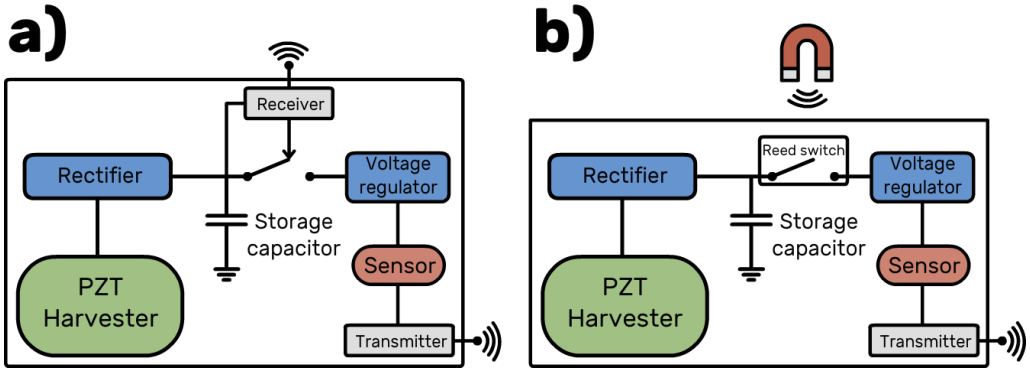

Figure 6.9: *Block diagram showing two variations of the proposed design of a piezoelectric harvester powering a sensor implant. A) Modes are switched when the receiver detects a wake-up signal. B) Modes are switched when the reed switch is exposed to a strong enough magnetic field.*

6.7 that the sensor's power consumption of $100 - 300\,\mu W$ far exceeds the PEH power output, even when accounting for the fact that the simulated ICP wave might be an underestimation. However, a receiver could enable the sensor to be inactive at all times except when a wake-up signal is received telling the system to start recording for a set duration, thereby significantly lowering the sensor power consumption (Figure 6.9 a). Alternatively, a reed switch, which can be switched on by placing a magnet close to the switch, could be used instead of a receiver (Figure 6.9 b) [65]. A reed switch is a completely passive component without any power consumption, however its range is generally lower than the range of a RF receiver. Such a system would cycle between two modes: a standby mode and an active mode. The harvester would be generating power continuously at all times to charge the storage capacitor. In standby mode, the wake-up receiver would be active, but the sensor and transceiver would be inactive. When a wake-up signal is received, the system would switch to active mode and the sensor and transceiver would be switched on for a set duration until the system goes back to standby mode. The wake-up receiver power consumption therefore constitutes a minimum power requirement which the harvester power output must meet. Transmitters for biomedical implants usually have a power consumption in the mW range, however various techniques have been suggested to achieve sub-mW low-power transmitters [66], [67], [68]. J. Pandey *et al.* utilized injection-locking to produce a transceiver unit for medical implants with a power consumption of $90\,\mu W$ [69]. Further, M. Zgaren *et al.*. demonstrated a passive wake-up receiver architecture where almost

all required power is harvested from the incoming wake-up signal, reducing the power consumption to only 0.2 µW [70].

Consequently, in standby mode, the system power consumption equals that of the wake-up receiver, 0.2 µW. In active mode, if the sensor's recorded data is sent continuously, the power consumption of the system equals that of the sensor and transceiver, which would amount to $200 - 400\,\mu W$. Thus, the wake-up receiver's power consumption constitutes a power consumption floor, which has to be matched by the PEH's power output. The average power output of the PEH simulated in this thesis is $P_{avg} = 2.6\,nW$, which is roughly two orders of magnitudes lower than the wake-up receiver's power consumption. Therefore, a wake-up receiver design would not be feasible, and a reed switch should be used instead.

The suggested harvesting strategy is described by the following two equations:

$$t_a \cdot P_c = (t_s + t_a)(P_h - P_L), \tag{13}$$

$$P_L = P_{L,rect} + P_{L,cap}. \tag{14}$$

P_c is the total power consumption of the system when it is in active mode, i.e. measuring and transmitting data and P_h is the power generated by the PEH. t_a and t_s is the time duration of the active mode and standby mode respectively, where $t_s >> t_a$ will be necessary when the PEH's power output is significantly lower than the system's power consumption in active mode. Various power losses in the system will have to be accounted for and these are represented by P_L. Next, the rectifier and storage unit will be discussed and their respective power losses $P_{L,rect}$ and $P_{L,cap}$ will be used to determine the overall power loss P_L of the system, as described by equation (14).

6.5.2 Rectifier

A rectifier is needed to convert the harvester output current from alternating current (AC) to direct current (DC), in order to charge the storage capacitor and to be compatible with the sensor which generally requires a DC input. There are different types of rectifiers, but full-wave center-tapped rectifiers are the most suitable for

low-power applications. Compared to a full-wave bridge rectifier, the current in a center-tapped rectifier only goes through one diode at a time, rather than two. Each diode results in a voltage drop which in turn causes a power loss equal to the voltage drop multiplied with the instantaneous current passing through the diode.

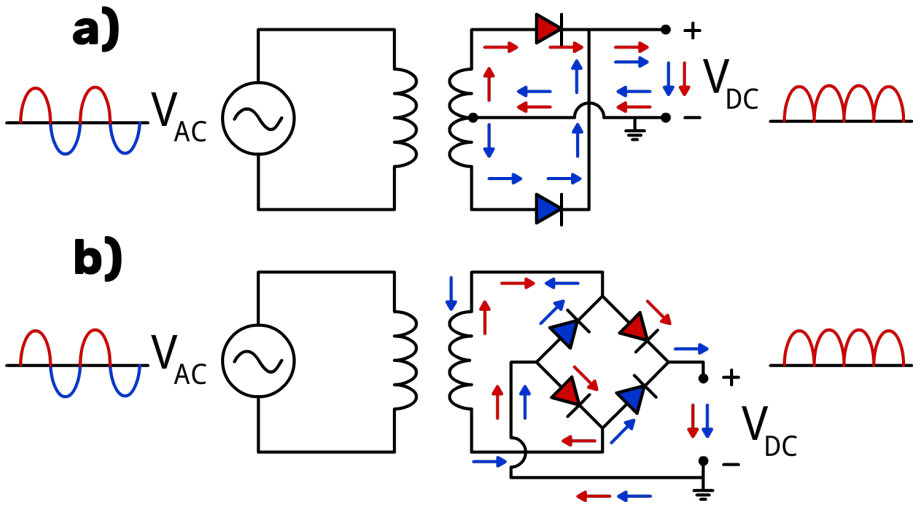

Figure 6.10: *Full-wave rectifier circuits. Red arrows show the current's direction during the positive cycle of the alternating current and blue arrows show the direction during the negative cycle. A) Full-wave center-tapped rectifier which uses two diodes and where the output is connected to the center of the secondary winding of the transformer. B) Full-wave bridge rectifier which uses four diodes.*

The primary and secondary winding of the rectifier's transformer can be adjusted to boost the low output voltage from the harvester to a voltage level compatible with the storage device, according to equation (15):

$$\frac{V_p}{V_s} = \frac{N_p}{N_s} = \frac{i_s}{i_p}. \tag{15}$$

V_p and N_p represent the voltage and winding number on the primary side while V_s and N_s represent the voltage and winding number on the secondary side. V_p and i_p equal the harvester output RMS voltage and output RMS current respectively, which can be calculated with equation (16):

$$V_p = V_{RMS} = \frac{V_{peak}}{\sqrt{2}}, \qquad i_p = i_{RMS} = \frac{i_{peak}}{\sqrt{2}}, \tag{16}$$

where the output peak voltage V_{peak} is the peak voltage shown in Figure 6.8 b). Thus, boosting the voltage to 3 V would require the winding ratio to be $\frac{N_p}{N_s} = 31$

if the PZT layers are connected in parallel and $\frac{N_p}{N_s} = 16$ if they are connected in series. Since the power does not change between the primary and secondary side, barring losses, the current would be lowered to $i_s = 0.69\,\text{nA}$ on the secondary side, as shown in equation (15). Then, the average power loss due to the voltage drop across a schottky diode with bias voltage $V_{bi} = 150\,\text{mV}$ would be $0.10\,\text{nW}$, according to equation (17):

$$P_{L,diode} = V_{bi} \cdot i_s = V_{bi} \cdot \sqrt{\frac{P_h}{R_L + R_D}}. \tag{17}$$

Additionally, with equation (16), (18) and (19):

$$\eta_{rect} = \frac{P_{DC} - P_{L,diode}}{P_h} = \frac{\frac{V_{DC}^2}{R_L} - P_{L,diode}}{\frac{V_{RMS}^2}{R_L + R_D}}, \tag{18}$$

$$V_{DC} = \frac{2}{\pi} V_{peak}, \tag{19}$$

the rectifier efficiency η_{rect} can be calculated. $P_h = 2.6\,\text{nW}$ is the average power generated by the harvester which is fed to the rectifier, while P_{DC} is the power of the rectifier output signal. R_L and R_D is the load resistance and the resistance in the diode respectively. Since the harvester requires a high load resistance, we can assume that $R_L >> R_D$. Further, as long as $V_{DC} >> V_{bi}$, we can assume that $P_{L,diode}$ is negligible. It would thus be suitable to use low bias schottky diodes. The equations can then be reduced to:

$$\eta_{rect} = \frac{\frac{V_{DC}^2}{R_L}}{\frac{V_{RMS}^2}{R_L}} = \frac{8}{\pi^2} \approx 0.81,$$

and consequently, the rectifier power loss can be calculated as:

$$P_{L,rect} = P_h(1 - \eta_{rect}). \tag{20}$$

6.5.3 Supercapacitor

The harvester might not generate enough power to drive a sensor implant continuously at all times. One alternative strategy could be to store the generated energy in some way, and then release it only during shorter measurements. One

potential storage unit is the supercapacitor, which has a longer lifetime than a chemical batteries, making it suitable for implanted systems [71]. Supercapacitors also exhibit very high power densities compared to batteries, but the energy density is only 5% of lithium batteries, meaning the amount of energy that can be stored is very limited for small-scale systems [17].

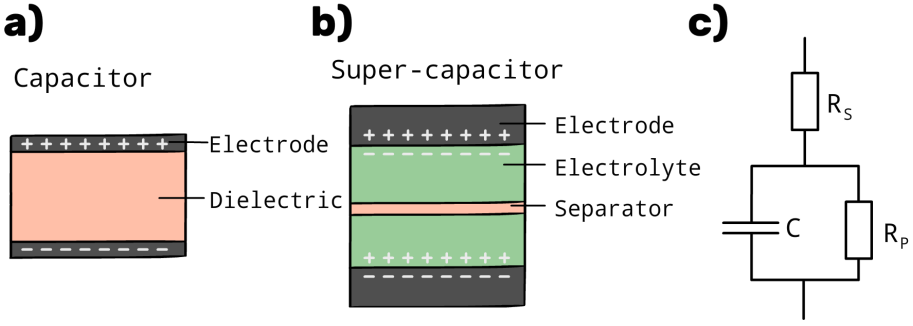

Figure 6.11: *a) A regular capacitor consisting of a dielectric material sandwiched between two electrodes. b) In a supercapacitor there is an electrolyte layer between the middle layer and each electrode. c) Equivalent circuit for a supercapacitor.*

A supercapacitor exhibit properties of a regular capacitor as well as properties of a conventional electrochemical battery. Two electrode plates are separated by an isolating layer, just like in a regular capacitor (see Figure 6.11). However, between the isolating layer and each plate is an electrolyte containing conducting ions, much like in an electrochemical battery [71]. The electrode-electrolyte interface on each end of a supercapacitor constitutes a capacitor in itself. The distance between the electrode's charge and the electrolyte's charge is very small, leading to a larger capacitance and a larger electric field than in regular capacitors. A larger electric field means that more energy can be stored. The amount of energy a capacitor can store is described by:

$$E_C = \frac{1}{2}CV^2. \tag{21}$$

However, supercapacitors have leakage currents. These may furthermore be enhanced by impurities in the electrodes or presence of oxygen in the electrolyte. Figure 6.11 c) shows an equivalent circuit for a supercapacitor. The resistor connected in parallel with the capacitance, R_P, is used to model the leakage current, while the resistor connected in series, R_S, represents internal resistance. The voltage drop across R_P can be described as an exponential decay of the voltage across the

supercapacitor V_{SC} [72]:

$$V(t) = V_{SC} e^{-\frac{1}{R_P C} t}.$$

Then, the leakage current going through R_P can be calculated:

$$i_{leak}(t) = \frac{V(t)}{R_P} = \frac{V_{SC}}{R_P} e^{-\frac{1}{R_P C} t},$$

and thus, we can see that as $t \to \infty$, the leakage current decreases. It can also be seen that higher capacitance C results in higher leakage currents. Supercapacitors can exhibit capacitance densities as large as $0.05 - 0.3\,\mathrm{F/cm^2}$ [73], which enables high energy densities. Using equation (21) and assuming $V = 3\,\mathrm{V}$, supercapacitors can achieve energy densities of $0.2 - 1.3\,\mathrm{J/cm^2}$. Let us consider an example to contextualize these energy densities. A pressure sensor and transmitter with a total power consumption of 300 µW could be powered for approximately 30 minutes by a fully charged $0.1\,\mathrm{cm^2}$ 0.15 F super capacitor.

However, since larger capacitance values generally imply larger leakage currents, there is a trade-off. In practice, 1 µA/F can be used as a rough guiding rule of thumb when estimating leakage currents in supercapacitors [74]. A supercapacitor specifically designed for low-power energy harvesting applications was recently presented by V. Gogolou *et al.*, with a leakage current of 0.4 µA and power loss of 1 µW [75]. P. Mars demonstrated another highly efficient 0.15 F capacitor which produced a very low leakage current of 0.2 µA [74]. However, if *e.g.* 3 V is supplied to the capacitor, even a small leakage current of 0.2 µA would amount to a power loss of 0.6 µW, which unfortunately far exceeds the power output of the PEH presented in this thesis. Also, leakage currents are generally significantly higher in the beginning when the capacitor is being charged and then they gradually decrease to reach their specified leakage current values. The previously mentioned 0.15 F capacitor's leakage current started at 20 µA and only reached its specified leakage current after 160 hours [74]. If the PEH's output current does not exceed the capacitor's leakage current, no charge will be accumulated and the harvesting system will not work. Thus, a system designed for high-current, low-voltage signals would likely be preferable.

Now, assuming $P_c = 300\,\mu\mathrm{W}$, $P_{L,cap} = 0.6\,\mu\mathrm{W}$ and $\eta_{rect} = 0.81$, equations (13) and (20) can be used to approximate the required harvester output for a given ratio of

$\delta = \frac{t_a}{t_s+t_a}$:

$$P_h = \frac{\delta P_c + P_{L,cap}}{\eta_{rect}} \approx 1.23(\delta 300 + 0.6)\ [\mu W]$$

Table IV shows the required harvester power outputs for and various measurement schemes. Note that as $\delta \to 0$, which means that measurements are taken more sparsely or are kept shorter, the expression can be simplified to $P_h \approx \frac{P_{L,cap}}{\eta_{rect}} \approx 0.74\,\mu W$.

Table IV: *Various suggested measurement schemes, with different duty cycles.*

δ	Measurement frequency	Required PEH output
0.02	30 min/day	8.12 µW
$7e^{-4}$	1 min/day	1.00 µW
$5e^{-5}$	30 s/week	0.76 µW
$2e^{-6}$	5 s/month	0.74 µW

7 Discussion

In this chapter, the results will be discussed and put into further context. Throughout this thesis, simplifications have been made when simulating complex structures or signals. Some components and aspects of the system design have been left out due to time constraint and prioritization. This chapter aims to briefly discuss these limitations and how they are likely to have affected the results. After that, suggestions are made for future research on the topic of piezoelectric energy harvesting from the human brain.

7.1 Power loss

The power loss in a rectifier as well as in a supercapacitor was estimated for a harvester-powered sensor implant. Since the required power output from the harvester approaches $P_h \approx \frac{P_{L,cap}}{\eta_{rect}}$ as $delta \to 0$, it is apparent that the leakage current of the supercapacitor largely determines the lower limit of the harvester's power output. In order to overcome the leakage current, the harvester's output must reach the order of µW.

While the rectifier and supercapacitor were the focus of this thesis regarding power

loss, there are other parts of the circuit which will have power losses, such as a voltage regulator connected between the capacitor and the sensor. There are also other effects that leakage current that leads to power loss in a supercapacitor, such as charge redistribution [72]. As mentioned earlier, the leakage current is actually significantly higher in the initial period when the capacitor begins to charge up. This phenomena was not included when deriving the values in table IV in chapter 6, meaning that the estimated required PEH outputs are likely underestimations.

When calculating the rectifier's efficiency, (16) and (19) only holds true if the harvester output is sinusoidal. This is true for the simulations in section 6.4, but the real ICP waveform is more complex, as seen in Figure 6.1. The rectifier's efficiency η_{rect} would thus likely be slightly different.

7.2 Simulated ICP

The power output in Figure 6.7 appears to grow quadratically with increasing pressure, which agrees with equations (9) - (11). This indicates that the pressure level is a key parameter which puts a strong limitation of the possible power output of an implantable harvester. The ICP pulsating pressure is difficult to estimate precisely, as the waveform is made up of shorter $\sim$ 3 mmHg pulses and longer $\sim$ 6 mmHg pulses (see Figure 6.1). Since the heart pulsating pressure is approximately 40 mmHg, the ratio between pulsating pressure in the heart and ICP pulsating pressure appears to be ten-fold. Due to the quadratic pressure dependency, the power density of a heart harvester could therefore be expected to be roughly two magnitudes larger than a brain harvester.

Since the slower variations of the ICP signal could not be simulated, it is likely that the simulated pressure variation of real$\{3e^{j0.94\cdot 2\pi\cdot t}\}$ mmHg is an underestimation and that the actual pressure variations in the brain are slightly larger. Furthermore, periods of elevated pressure and higher frequency such as shown in Figure 6.1 b) would significantly increase the harvester output.

The brain cylinder used during the FEM simulations is a very rudimentary model. The model assumes that all pressure is exerted from the brain ventricles which are located underneath the cylinder. In a real human brain, CSF does not only exists

inside of the ventricles. CSF perforates the brain via vessels and flows outside of the brain surface as well, in the *subarachnoid* space [4]. On top of that there are blood vessels lining the brain surface, which also pulsate. If one managed to include these structures in simulations, it is likely that the harvester output would increase, since one would in practice add a network of additional smaller pressure sources. A brain model with only the ventricles as a pressure source might not be a sufficient model for estimating the PEH output. This could also explain why the test-rig silicone brain did not show any response when its artificial ventricle was pressurized.

7.3 Test rig performance

The initial strategy of constructing the silicone phantom brain by gluing two halves together yielded poor results as the glue formed scarring on the phantom surface, and risked clogging the tubes. The hardened cyanoacrylate glue was also much more brittle than the silicone and therefore cracks formed in the glue, leading to leaking. By constructing the phantom using a main body and a much smaller lid piece, rather than two equally sized halves, less surface area required bonding. Furthermore, bonding the pieces with silicone rather than glue yielded a more smooth and less brittle phantom. The final phantom brain did not show any leakage, and water was transported through it successfully. However, no mechanical expansion or constriction was observed in the phantom. The pressure system displayed a strong inertia which made it impossible to induce rapid pressure changes in the phantom brain. The frequency was lowered to 0.2 Hz but still only small pressure fluctuations were observed.

7.4 Suggestions for future research

It would be interesting to see how much the simplifications of the modelled brain cylinder impacted the harvester performance during simulations. Better understanding of the pressure dynamics inside the human brain as well as more computation power would enable a more advanced and realistic FEM brain model to be constructed. For example, in Comsol, the simulations were performed as a *frequency study*. There is also a *time study* function, but this was not used as it was too computationally demanding. With more computation power however, this

could potentially be used to stimulate more complex pressure signals, in order to mimic the real ICP waveform.

The design of the thin plate harvester itself could be seen as a proof-of-concept model, indicating what a relatively simple cantilever harvester could harvest from the human brain. The *in vivo* harvesters presented in chapter 4 shows how reported power densities have increased from 24 nW/cm^3 to 138 µW/cm^3 since 2008. Thus, even if the power output of the harvester simulated in this thesis is significantly lower than the mW requirement, more research should be devoted to explore more complex harvester structures such as nanowire arrays and nanoribbons. Also, promising emerging piezoelectric composites such as PMN-PZT and PVDF-ZnO should also be evaluated in a brain harvesting application. Since the pressure appears to be one of the main limiting factors regarding brain harvesting, it would also be interesting to explore piezoelectric harvesting from larger arteries situated near the brain in order to power brain implants.

One important aspect of medical implants is biocompatibility. An implanted harvester device would most likely need some form of incapsulation, especially if it is made from toxic materials such as lead which is found in PZT. This is a major reason why other piezoelectric ceramics such as ZnO or polymers such as PVDF are being subjected to research today. However, if the power output of lead-free brain harvesters fail to reach the same power output as a PZT harvester, there will be a trade-off between biocompatibility and power output. Even if one might initially gravitate towards favouring biocompatibility, it has been shown in this thesis that the mechanical power available from the brain is much lower than that of the heart and so, one might not afford to make any concessions regarding power output. First and foremost the most efficient harvesting material should be found, and then effort should be put into ensuring the biocompatibility of harvesters made form that material.

7.5 Conclusion

It has been shown from calculations and simulations that the power output of a PEH harvesting from a pulsating organ has a quadratic dependency on the pulsating

pressure. Thus, since the pulsating pressure of the human brain is significantly lower than the pressure of the heart, one should expect there to be a significant discrepancy between piezoelectric brain- and heart-harvesting output. This discrepancy could be as large as two orders ofmagnitude. A PZT thin plate harvester was simulated and displayed an optimal average power output of 2.6 nW. The harvester was made up of a cantilever plate consisting of two 50 µm PZT layers sandwiched between two 100 nm electrodes, with an additional middle electrode for the parallel configuration. The most realistic strategy for powering an ICP sensor implant by harvesting from the brain would be to only measure and transmit data periodically for a short duration. Measuring for one minute per day would require a harvester output of approximately 1 µW. The supercapacitor leakage current is the main source of power loss which must be overcome and thus it seems that a brain harvester must produce an output power of at least one µW in order for piezoelectric brain harvesting to be feasible. The theoretical power output limit for a PZT harvester, accounting for its coupling factor, is approximately 1.4 µW.

References

[1] D. Pickering and S. Stevens. "How to measure and record blood pressure." In: *Community eye health* 26.84 (Jan. 2013), p. 76. ISSN: 1993-7288. [Online].Available: https://www.ncbi.nlm.nih.gov/pmc/articles/PMC3936692/.

[2] N. Canac et al. "Review: pathophysiology of intracranial hypertension and noninvasive intracranial pressure monitoring." In: *Fluids and barriers of the CNS* 17.1 (June 2020), p. 40. ISSN: 2045-8118. DOI: 10.1186/s12987-020-00201-8.

[3] K. Ladislav. "The 20 W sleep-walkers". In: *EMBO reports* 11.1 (Jan. 2010), p. 2. ISSN: 1469-3178. DOI: 10.1038/embor.2009.266.

[4] G. J. Tortora and B. Derrickson. *Introduction to the Human Body*. Ed. by M. Guarascio. 11th ed. Glasgow, Great Britain: John Wiley & Sons, Inc., 2019, p. 245.

[5] M. Harary, R. G. F. Donalds, and W. B. Gormley. "Intracranial Pressure Monitoring-Review and Avenues for Development". In: *Sensors (Basel)* 18.2 (Feb. 2018), p. 465. ISSN: 1424-8220. DOI: 10.3390/s18020465.

[6] S. M. Nehring, P. Tadi, and S. Tenny. "Cerebral Edema". In: *StatPearls [Internet]*. StatPearls Publishing, 2022. [Online].Available: https://www.ncbi.nlm.nih.gov/books/NBK537272/. (Accessed:2023.04.26).

[7] N. Sezer and M. Koç. "A comprehensive review on the state-of-the-art of piezoelectric energy harvesting". In: *Nano Energy* 80 (Feb. 2021), p. 105567. ISSN: 2211-2855. DOI: 10.1016/j.nanoen.2020.105567.

[8] A. Vyas. *On-chip electrochemical capacitors and piezoelectric energy harvesters for self-powering sensor nodes*. Göteborg, Sweden: Chalmers University of Technology, 2022.

[9] Y. Zou, L. Bo, and Z. Li. "Recent progress in human body energy harvesting for smart bioelectronic system". In: *Fundamental Research* 1.3 (May 2021), pp. 364–382. ISSN: 2667-3258. DOI: 10.1016/j.fmre.2021.05.002.

[10] R. Li et al. “Harvesting energy from pavement based on piezoelectric effects: Fabrication and electric properties of piezoelectric vibrator”. In: *Journal of Renewable and Sustainable Energy* 10.5 (Sept. 2018), p. 054701. DOI: 10.1063/1.5002731.

[11] Y. Song et al. “Road energy harvester designed as a macro-power source using the piezoelectric effect”. In: *International Journal of Hydrogen Energy* 41.29 (2016), pp. 12563–12568. ISSN: 0360-3199. DOI: https://doi.org/10.1016/j.ijhydene.2016.04.149.

[12] B. Orr et al. “A review of car waste heat recovery systems utilising thermoelectric generators and heat pipes”. In: *Applied Thermal Engineering* 101 (2016), pp. 490–495. ISSN: 1359-4311. DOI: https://doi.org/10.1016/j.applthermaleng.2015.10.081.

[13] S. Azimi et al. “Self-powered cardiac pacemaker by piezoelectric polymer nanogenerator implant”. In: *Nano Energy* 83 (May 2021), p. 105781. ISSN: 2211-2855. DOI: 10.1016/j.nanoen.2021.105781.

[14] A. N. Sadr et al. “Evaluation of Energy Harvesting from Different Sections of the Aortic Artery with Several Energy Harvester Materials”. In: *Advanced Materials Technologies* (June 2022), p. 2100986. ISSN: 2365-709X. DOI: 10.1002/admt.202100986.

[15] J. A. Potkay and K. Brooks. “An Arterial Cuff Energy Scavenger For Implanted Microsystems”. In: *2008 2nd International Conference on Bioinformatics and Biomedical Engineering*. 2008, pp. 1580–1583. DOI: 10.1109/ICBBE.2008.723.

[16] D. Leeth et al. “Normothermia and patient comfort: a comparative study in an outpatient surgery setting.” In: *Journal of perianesthesia nursing : official journal of the American Society of PeriAnesthesia Nurses* 25.3 (June 2010), pp. 146–151. ISSN: 1089-9472. DOI: 10.1016/j.jopan.2010.03.010.

[17] S. Roy et al. “Powering Solutions for Biomedical Sensors and Implants Inside the Human Body: A Comprehensive Review on Energy Harvesting Units, Energy Storage, and Wireless Power Transfer Techniques”. In: *IEEE Transactions on Power Electronics* 37.10 (Oct. 2022), pp. 12237–12263. ISSN: 1941-0107. DOI: 10.1109/TPEL.2022.3164890.

[18] H. X. Q. Yang, D. Wang, and W. Luo. “A wearable pyroelectric nanogenerator and self-powered breathing sensor”. In: *Nano Energy* 38 (Aug. 2017), pp. 147–154. ISSN: 2211-2855. DOI: 10.1016/j.nanoen.2017.05.056.

[19] D. H. Kim et al. “In Vivo Self-Powered Wireless Transmission Using Biocompatible Flexible Energy Harvesters”. In: *Advanced Functional Materials* 27.25 (2017), p. 1700341. DOI: https://doi.org/10.1002/adfm.201700341.

[20] M. A. P. Mahmud et al. “Recent Advances in Nanogenerator-Driven Self-Powered Implantable Biomedical Devices”. In: *Advanced Energy Materials* 8.2 (Sept. 2017), p. 1701210. ISSN: 1614-6832. DOI: 10.1002/aenm.201701210.

[21] C. R. Bowen et al. “Piezoelectric and ferroelectric materials and structures for energy harvesting applications”. In: *Energy Environ. Sci.* 7 (1 2014), pp. 25–44. DOI: 10.1039/C3EE42454E.

[22] Q. Zheng et al. “Recent Progress on Piezoelectric and Triboelectric Energy Harvesters in Biomedical Systems”. In: *Recent Progress on Piezoelectric and Triboelectric Energy Harvesters in Biomedical Systems* 4.7 (Mar. 2017), pp. 2198–3844. ISSN: 2198-3844. DOI: 10.1002/advs.201700029.

[23] H. Hoshyarmanesh and Y. Maddahi. “Poling Process of Composite Piezoelectric Sensors for Structural Health Monitoring: A Pilot Comparative Study”. In: *IEEE Sensors Letters* 2.1 (2018), pp. 1–4. DOI: 10.1109/LSENS.2018.2806301.

[24] Z. Wang et al. “Piezoelectric Nanowires in Energy Harvesting Applications”. In: *Advances in Materials Science and Engineering* (June 2015), p. 165631. ISSN: 1687-8434. DOI: 10.1155/2015/165631.

[25] S. R. Platt, S. Farritor, and H. Haider. “On low-frequency electric power generation with PZT ceramics”. In: *IEEE/ASME Transactions on Mechatronics* 10.2 (Apr. 2005), pp. 240–252. ISSN: 1941-014X. DOI: 10.1109/TMECH.2005.844704.

[26] R. M. Chesnut et al. “A Trial of Intracranial-Pressure Monitoring in Traumatic Brain Injury”. In: *New England Journal of Medicine* 367.26 (Dec. 2012), pp. 2471–2481. ISSN: 0028-4793. DOI: 10.1056/NEJMoa1207363.

[27] A. Tang et al. “Intracranial pressure monitor in patients with traumatic brain injury”. In: *Journal of Surgical Research* 194.2 (Apr. 2015), pp. 565–570. ISSN: 0022-4804. DOI: 10.1016/j.jss.2014.11.017.

[28] A. Schütze et al. “Design and Optimization of a Low Power Pressure Sensor for Wireless Biomedical Applications”. In: *Journal of Sensors* 2015 (Sept. 2015), p. 352036. ISSN: 1687-725X. DOI: 10.1155/2015/352036.

[29] P. Cong et al. “A Wireless and Batteryless 10-Bit Implantable Blood Pressure Sensing Microsystem With Adaptive RF Powering for Real-Time Laboratory Mice Monitoring”. In: *IEEE Journal of Solid-State Circuits* 44.12 (2009), pp. 3631–3644. DOI: 10.1109/JSSC.2009.2035551.

[30] B. Ziaie and K. Najafi. “An Implantable Microsystem for Tonometric Blood Pressure Measurement”. In: *Biomedical Microdevices* 3.4 (Dec. 2001), pp. 285–292. ISSN: 1572-8781. DOI: 10.1023/A:1012452613720.

[31] Z. Li et al. “Muscle-Driven In Vivo Nanogenerator”. In: *Advanced Materials* 22.23 (June 2010), pp. 2534–2537. ISSN: 0935-9648. DOI: 10.1002/adma.200904355.

[32] S. Bhalla et al. *Piezoelectric Materials : Applications in SHM, Energy Harvesting and Biomechanics*. Chichester, United Kingdom: John Wiley & Sons, Inc., 2017.

[33] S. Crossley and S. Kar-Narayan. “Energy harvesting performance of piezoelectric ceramic and polymer nanowires”. In: *Nanotechnology* 26.34 (Aug. 2015), p. 344001. ISSN: 0957-4484. DOI: 10.1088/0957-4484/26/34/344001.

[34] K. Uchino. “The development of piezoelectric materials and the new perspective”. In: *Advanced Piezoelectric Materials*. Woodhead Publishing, 2010. Chap. 1, pp. 1–85. DOI: 10.1533/9781845699758.1.

[35] Y. Yan et al. “Giant piezoelectric voltage coefficient in grain-oriented modified PbTiO3 material”. In: *Nature Communications* 7.1 (Oct. 2016), p. 13089. ISSN: 2041-1723. DOI: 10.1038/ncomms13089.

[36] M. A. Fraga et al. “Wide bandgap semiconductor thin films for piezoelectric and piezoresistive MEMS sensors applied at high temperatures: an overview”. In: *Microsystem Technologies* 20.1 (Jan. 2014), pp. 9–21. ISSN: 1432-1858. DOI: 10.1007/s00542-013-2029-z.

[37] S. Kuchipudi, P. Goduru, and S. Suryanarayana. “Piezoelectric characterization of Ferrite/Ferroelectric magnetoelectric composite system”. In: *Modern Physics Letters B* 14.17 & 18 (Mar. 2001), pp. 663–674. DOI: 10.1142/S021798490000080X.

[38] Y. Jiang et al. “Low-frequency energy harvesting using a laminated PVDF cantilever with a magnetic mass”. In: 2010.

[39] C. Miclea. “Preparation of Piezoelectric Nanoparticles”. In: *Piezoelectric Nanomaterials for Biomedical Applications*. Ed. by G. Ciofani and A. Menciassi. Berlin, Heidelberg: Springer Berlin Heidelberg, 2012. Chap. 2, pp. 29–61. DOI: 10.1007/978-3-642-28044-3_2.

[40] L. Jiang et al. “Flexible piezoelectric ultrasonic energy harvester array for bio-implantable wireless generator”. In: *Nano Energy* 56 (Feb. 2019), pp. 216–224. ISSN: 2211-2855. DOI: 10.1016/j.nanoen.2018.11.052.

[41] Q.-M. Wang et al. “Theoretical analysis of the sensor effect of cantilever piezoelectric benders”. In: *Journal of Applied Physics* 85 (Feb. 1999), pp. 1702–1712. DOI: 10.1063/1.369314.

[42] A. Kubba and K. Jiang. “A Comprehensive Study on Technologies of Tyre Monitoring Systems and Possible Energy Solutions”. In: *Sensors (Basel, Switzerland)* 14 (June 2014), pp. 10306–10345. DOI: 10.3390/s140610306.

[43] S. Du et al. “A new electrode design method in piezoelectric vibration energy harvesters to maximize output power”. In: *Sensors and Actuators A: Physical* 263 (2017), pp. 693–701. ISSN: 0924-4247. DOI: https://doi.org/10.1016/j.sna.2017.06.026.

[44] B. Li et al. “Self-polarized piezoelectric thin films: preparation, formation mechanism and application”. In: *J. Mater. Chem. C* 3 (34 2015), pp. 8926–8931. DOI: 10.1039/C5TC01869B.

[45] W. Wu. "High-performance piezoelectric nanogenerators for self-powered nanosystems: quantitative standards and figures of merit". In: *Nanotechnology* 27.11 (Feb. 2016), p. 112503. ISSN: 0957-4484. DOI: 10.1088/0957-4484/27/11/112503.

[46] C. Falconi et al. "Modeling of Piezoelectric Nanodevices". In: *Piezoelectric Nanomaterials for Biomedical Applications*. Ed. by G. Ciofani and A. Menciassi. Berlin, Heidelberg: Springer Berlin Heidelberg, 2012. Chap. 4, pp. 93–133. DOI: 10.1007/978-3-642-28044-3_4.

[47] C. K. Jeong et al. "Comprehensive biocompatibility of nontoxic and high-output flexible energy harvester using lead-free piezoceramic thin film". In: *APL Materials* 5.7 (Feb. 2017). ISSN: 2166-532X. DOI: 10.1063/1.4976803.

[48] C. Dagdeviren et al. "Conformal piezoelectric energy harvesting and storage from motions of the heart, lung, and diaphragm". In: *Proceedings of the National Academy of Sciences* 111.5 (2014), pp. 1927–1932. DOI: 10.1073/pnas.1317233111.

[49] G.-T. Hwang et al. "Self-Powered Cardiac Pacemaker Enabled by Flexible Single Crystalline PMN-PT Piezoelectric Energy Harvester". In: *Advanced Materials* 26.28 (Apr. 2014), pp. 4880–4887. DOI: 10.1002/adma.201400562.

[50] B. Lu et al. "Ultra-flexible Piezoelectric Devices Integrated with Heart to Harvest the Biomechanical Energy". In: *Scientific Reports* 5.1 (Nov. 2015), p. 16065. ISSN: 2045-2322. DOI: 10.1038/srep16065.

[51] H. Zhang et al. "A flexible and implantable piezoelectric generator harvesting energy from the pulsation of ascending aorta: in vitro and in vivo studies". In: *Nano Energy* 12 (2015), pp. 296–304. ISSN: 2211-2855. DOI: 10.1016/j.nanoen.2014.12.038.

[52] X. Cheng et al. "Implantable and self-powered blood pressure monitoring based on a piezoelectric thinfilm: Simulated, in vitro and in vivo studies". In: *Nano Energy* 22 (2016), pp. 453–460. ISSN: 2211-2855. DOI: 10.1016/j.nanoen.2016.02.037.

[53] L. Beker et al. "Energy harvesting from cerebrospinal fluid pressure fluctuations for self-powered neural implants". In: *Biomedical Microdevices* 19.2 (Apr. 2017), p. 32. ISSN: 1572-8781. DOI: 10.1007/s10544-017-0176-1.

[54] L. Dong et al. “Flexible Porous Piezoelectric Cantilever on a Pacemaker Lead for Compact Energy Harvesting”. In: *Advanced Materials Technologies* 4.1 (Sept. 2019), p. 1800148. DOI: 10.1002/admt.201800148.

[55] Z. Xu et al. “Flexible Energy Harvester on a Pacemaker Lead Using Multibeam Piezoelectric Composite Thin Films”. In: *ACS Applied Materials & Interfaces* 12.30 (2020), pp. 34170–34179. DOI: 10.1021/acsami.0c07969.

[56] P. D. Mitcheson et al. “Energy Harvesting From Human and Machine Motion for Wireless Electronic Devices”. In: *Proceedings of the IEEE* 96.9 (2008), pp. 1457–1486. DOI: 10.1109/JPROC.2008.927494.

[57] D. Farahmand et al. “Intracranial pressure in hydrocephalus: impact of shunt adjustments and body positions.” In: *J Neurol Neurosurg Psychiatry* 86.2 (Feb. 2015), pp. 222–8. ISSN: 0022-3050. DOI: 10.1136/jnnp-2014-307873.

[58] C. Chourpiliadis and A. Bhardwaj. “StatPearls”. In: *Physiology, Respiratory Rate.* StatPearls Publishing, 2022. [Online].Available: https://www.ncbi.nlm.nih.gov/books/NBK537306/. (Accessed:2023.05.16).

[59] I. Martinez-Tejada et al. “B waves: a systematic review of terminology, characteristics, and analysis methods”. In: *Fluids and Barriers of the CNS* 16.1 (Oct. 2019), p. 33. ISSN: 2045-8118. DOI: 10.1186/s12987-019-0153-6.

[60] P. Portella et al. “Continuous cerebral compliance monitoring in severe head injury: its relationship with intracranial pressure and cerebral perfusion pressure”. In: *Acta Neurochirurgica* 147.7 (July 2005), pp. 707–713. ISSN: 0942-0940. DOI: 10.1007/s00701-005-0537-z.

[61] H. Lemaitre et al. “Normal age-related brain morphometric changes: nonuniformity across cortical thickness, surface area and gray matter volume?” In: *Neurobiology of Aging* 33.3 (Mar. 2012), 617.e1–617.e9. ISSN: 0197-4580. DOI: 10.1016/j.neurobiolaging.2010.07.013.

[62] C. Henery and T. M. Mayhew. “The cerebrum and cerebellum of the fixed human brain: efficient and unbiased estimates of volumes and cortical surface areas.” In: *Journal of anatomy* 167 (Dec. 1989), pp. 167–180. ISSN: 0021-8782.

[63] R. Wang, E. Tang, and G. Yang. "Dynamic Piezoelectric Properties of PZT-5H Under Shock Compression". In: *physica status solidi (a)* 216.6 (2019), p. 1800859. DOI: 10.1002/pssa.201800859.

[64] D. Cederberg, N. Marklund, and R. H. Nittby. "Extreme intracranial pressure elevation > 90 mmHg in an awake patient with primary CNS lymphoma-case report." In: *Acta neurochirurgica* 162.8 (Aug. 2020). ISSN: 0001-6268. DOI: 10.1007/s00701-020-04231-x.

[65] H. Ouyang et al. "Symbiotic cardiac pacemaker". In: *Nature Communications* 10.1 (Apr. 2019), p. 1821. ISSN: 2041-1723. DOI: 10.1038/s41467-019-09851-1.

[66] S.-J. Yun et al. "A Low Power Fully Intergrated RF Transceiver for Medical Implant Communication". In: *2018 IEEE International Symposium on Circuits and Systems (ISCAS)*. 2018, pp. 1–4. DOI: 10.1109/ISCAS.2018.8351197.

[67] T. Copani et al. "A CMOS Low-Power Transceiver With Reconfigurable Antenna Interface for Medical Implant Applications". In: *IEEE Transactions on Microwave Theory and Techniques* 59.5 (2011), pp. 1369–1378. DOI: 10.1109/TMTT.2011.2116036.

[68] P. D. Bradley. "An ultra low power, high performance Medical Implant Communication System (MICS) transceiver for implantable devices". In: *2006 IEEE Biomedical Circuits and Systems Conference*. 2006, pp. 158–161. DOI: 10.1109/BIOCAS.2006.4600332.

[69] J. Pandey and B. P. Otis. "A Sub-100 μ W MICS/ISM Band Transmitter Based on Injection-Locking and Frequency Multiplication". In: *IEEE Journal of Solid-State Circuits* 46.5 (2011), pp. 1049–1058. DOI: 10.1109/JSSC.2011.2118030.

[70] M. Zgaren and M. Sawan. "A Low-Power Dual-Injection-Locked RF Receiver With FSK-to-OOK Conversion for Biomedical Implants". In: *IEEE Transactions on Circuits and Systems I: Regular Papers* 62.11 (2015), pp. 2748–2758. DOI: 10.1109/TCSI.2015.2477577.

[71] Q. Li. *Electrochemical capacitors for miniaturized self-powered systems: challenges and solutions*. Göteborg, Sweden: Chalmers University of Technology, 2020.

[72] S. Kim and P. H. Chou. “Energy Harvesting with Supercapacitor-Based Energy Storage”. In: *Smart Sensors and Systems*. Ed. by Y.-L. Lin et al. Cham: Springer International Publishing, 2015, pp. 215–241. ISBN: 978-3-319-14711-6. DOI: 10.1007/978-3-319-14711-6_10.

[73] J. keskinen et al. “Architectural modifications for flexible supercapacitor performance optimization”. In: *Electronic Materials Letters* 12.6 (Nov. 2016), pp. 795–803. ISSN: 2093-6788. DOI: 10.1007/s13391-016-6141-y.

[74] P. Mars. “Coupling a supercapacitor with a small energyharvesting source”. In: *EDN* 57 (June 2012), pp. 39–42.

[75] V. Gogolou et al. “An Ultra-Low-Power CMOS Supercapacitor Storage Unit for Energy Harvesting Applications”. In: *Electronics* 10.17 (Aug. 2021), p. 2097. ISSN: 2079-9292. DOI: 10.3390/electronics10172097.